Cronfa - Swansea University Open Access Repository

_____

This is an author produced version of a paper published in:
Journal of Computational Physics

_____

Cronfa URL for this paper:

_____

Paper:

_____

Accepted Manuscript

CVD-MPFA full pressure support, coupled unstructured discrete fracture-matrix Darcy-flux approximations

Raheel Ahmed, Michael G. Edwards, Sadok Lamine, Bastiaan A.H. Huisman, Mayur Pal
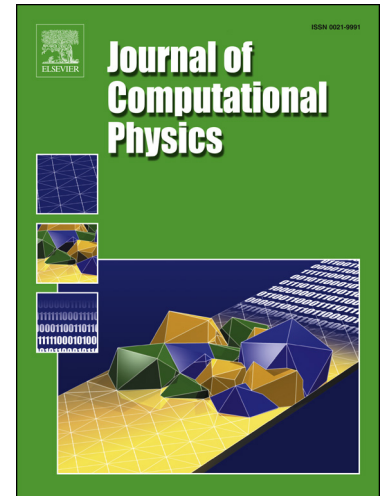
Please cite this article in press as: R. Ahmed et al., CVD-MPFA full pressure support, coupled unstructured discrete fracture-matrix Darcy-flux approximations, *J. Comput. Phys.* (2017), http://dx.doi.org/10.1016/j.jcp.2017.07.041

CVD-MPFA full pressure support, coupled unstructured discrete fracture-matrix Darcy-flux approximations

Raheel Ahmed[a,*], Michael G. Edwards[a], Sadok Lamine[b], Bastiaan A.H. Huisman[b], Mayur Pal[c]

[a]*ZCCE, College of Engineering, Swansea University, Bay Campus, Swansea SA1 8EN, Wales UK*
[b]*Shell Global Solutions International B.V., Kessler Park 1, 2288 GS, Rijswijk, The Netherlands.*
[c]*Maersk Oil and Gas A/S, 1263 Copenhagen, Denmark.*

Abstract

Two novel control-volume methods are presented for flow in fractured media, and involve coupling the control-volume distributed multi-point flux approximation (CVD-MPFA) constructed with full pressure support (FPS), to two types of discrete fracture-matrix approximation for simulation on unstructured grids; (i) involving hybrid grids and (ii) a lower dimensional fracture model. Flow is governed by Darcy's law together with mass conservation both in the matrix and the fractures, where large discontinuities in permeability tensors can occur. Finite-volume FPS schemes are more robust than the earlier CVD-MPFA triangular pressure support (TPS) schemes for problems involving highly anisotropic homogeneous and heterogeneous full-tensor permeability fields. We use a cell-centred hybrid-grid method, where fractures are modelled by lower-dimensional interfaces between matrix cells in the physical mesh but expanded to equi-dimensional cells in the computational domain. We present a simple procedure to form a consistent hybrid-grid locally for a dual-cell. We also propose a novel hybrid-grid for intersecting fractures, for the FPS method, which reduces the condition number of the global linear system and leads to larger time steps for tracer transport. The transport equation for tracer flow is coupled with the pressure equation and provides flow parameter assessment of the fracture models. Transport results obtained via TPS and FPS hybrid-grid formulations are compared with the corresponding results of fine-scale explicit equi-dimensional formulations. The results show that the hybrid-grid FPS method applies to general full-tensor fields and provides improved robust approximations compared to the hybrid-grid TPS method for fractured domains, for both weakly anisotropic permeability fields and very strong anisotropic full-tensor permeability fields where the TPS scheme exhibits spurious oscillations. The hybrid-grid FPS formulation is extended to compressible flow and the results demonstrate the method is also robust for transient flow.

Furthermore, we present FPS coupled with a lower-dimensional fracture model, where fractures are strictly lower-dimensional in the physical mesh as well as in the computational domain. We present a comparison of the hybrid-grid FPS method and the lower-dimensional fracture model for several cases of isotropic and anisotropic fractured media which illustrate the benefits of the respective methods.

*Corresponding author
Email addresses: R.AHMED.642142@swansea.ac.uk (Raheel Ahmed), m.g.edwards@swansea.ac.uk (Michael G. Edwards)

1. Introduction

A number of approaches have been proposed in the literature for coupling various finite-element and finite-volume methods with discrete-fracture based methods (DFM) for modelling fluid flow through fractured porous media. In the discrete-fracture method (DFM) see e.g. [1–13] actual orientation and location of the fractures are honoured in the domain. Unlike the dual-porosity model [14–17], the effect of individual fractures on fluid flow can be determined and fluid transfer between the fracture and matrix is more straightforward and consistent. Generally, fractures are modelled by (n-1) dimensional elements in an n-dimensional domain, for example in 2D, fractures are represented by lines which coincide with edges of polygonal matrix elements. An unstructured grid is used to honour the explicit fracture geometry where grid cells can be boundary aligned with fractures (see [18, 19]). Equi-dimensional representation of fractures [20], are not popular because of complexity and computational cost contributed by thin cells. Recently, different techniques of flow approximation in a discrete-fracture-matrix system have been presented. Finite element and extended-finite element (XFEM) methods for embedded fractures into non-conforming meshes are presented in [21–23]. Mixed hybridized finite-element (MHFE) and discontinous Galerkin (DG) methods [10] are presented for multicomponent compressible flow in [24–27]. Other recent methods for discrete fracture model simulations include the mimetic finite-difference method [28] and the vertex-approximate-gradient (VAG) method [29, 30].

Recently, Sandve et. al. [31] presented discrete-fracture and matrix simulations based on the hybrid-grid approach [6] using a multi-point flux approximation (MPFA) [32]. In the hybrid-grid method, fractures are (n-1)D in the physical mesh and are expanded to nD in the computational domain, resulting in efficient gridding of fractures. The nD pressure equation is solved by the default CVD-MPFA method in both matrix and fractures in the computational domain. The main difference in computational efficiency between the equi-dimensional model and the hybrid-grid model is the treatment of intermediate cells between intersecting fractures. In the hybrid-grid method of [31], the intermediate cell is assumed to be of small size so that pressure variation is zero in that cell to avoid the complexity that would be incurred by the small size of the intermediate cell in the equi-dimensional model.

In the work presented here, CVD-MPFA full pressure support (FPS) schemes are coupled with (i) the hybrid-grid method and (ii) a lower-dimensional fracture model for fracture-matrix simulations, leading to two novel FPS based formulations for modelling flow in fractured media. Coupling of CVD-MPFA triangle pressure support (TPS) schemes with lower-dimensional fracture models is presented in [33, 34].

TPS finite-volume methods are presented in [35, 36], with the TPS default quadrature case ($q = 1$) corresponding to MPFA methods, [32] on triangles and [37] on quads and with related methods [38, 39]. The TPS methods have proven effective for problems with lower manisotropies. However, the TPS methods can yield results with strong spurious oscillations for challenging non-linear test cases involving strongly anisotropic

2

35 full-tensor fields. The TPS methods have been shown to permit decoupled solution modes for such cases, and while both the TPS and FPS methods are shown to violate M-matrix conditions in such cases and indeed all such linear methods have an M-matrix condition dependent local discrete maximum principle (LDMP), the FPS methods prevent decoupled modes and yield well resolved pressure fields that are free of the accompanying grid level spurious oscillation modes [40–42]. Alternative related approaches are presented

40 in [43, 44], however only non-linear finite-volume methods [45, 46] have the facility for ensuring a discrete maximum principle for such problems, but these methods require solution via additional iterative techniques. In contrast FPS results in a classical linear algebraic system to be solved for discrete pressures and therefore does not involve the additional computational complexity associated with non-linear methods. Details of coupling the FPS formulation to both hybrid grids and lower dimensional fracture models are

45 presented here together with results comparing the earlier TPS and FPS fracture formulations. The hybrid grid FPS formulation is also extended to compressible flow and the result demonstrates that the method is also robust for transient flow.

The outline of the paper is as follows. We start with a description of flow equations for single-phase fluid

50 flow through porous media in section 2. We briefly describe the CVD-MPFA schemes for porous media in section 3. The hybrid-grid TPS and FPS methods for fractured porous media are described in section 4. Numerical results are presented in section 5 where the hybrid-grid TPS and FPS methods are compared. We present FPS coupled with a lower-dimensional fracture model and its comparison with hybrid-grid FPS method in section 6 before concluding in section 7.

55 ## 2. Flow equations

In this work we consider approximation of both elliptic and parabolic equations for pressure. The parabolic case arises for compressible flow and is considered in section 5.7. Our main focus here is on the discretisation of an elliptic partial differential equation for pressure. The pressure equation arises from Darcy's law and mass conservation ($\nabla \cdot \boldsymbol{v} = q_c$) for an incompressible single phase flow, (a similar method is

60 also applicable to multiphase flow). The resulting elliptic pressure equation

$$-\nabla \cdot \frac{\boldsymbol{k}}{\mu} \nabla \phi = q_c \qquad (1)$$

is solved on a domain Ω, where q_c is any known source term. As usual in single phase flow we let $\boldsymbol{K} = \frac{\boldsymbol{k}}{\mu}$ denote the (abbreviated) possibly heterogeneous spatially varying, symmetric permeability tensor, which can be full or diagonal and is generally expressed as: $\boldsymbol{K} = \left(\begin{smallmatrix} K_{11} & K_{12} \\ K_{12} & K_{22} \end{smallmatrix} \right)$ with respect to Cartesian axes. Equation (1) is solved here subject to Dirichlet and/or Neumann boundary conditions where $\phi = h(\boldsymbol{x})$ and

65 $(\boldsymbol{K}\nabla\phi) \cdot \boldsymbol{n} = g(\boldsymbol{x})$ respectively on the domain boundary $\delta\Omega$, where h and g are scalar fields defined on specified boundaries and $\boldsymbol{n}$ is the normal vector at the boundary.

3

The general permeability tensor of a fracture is written in Cartesian axes as $\boldsymbol{K_f} = \begin{pmatrix} K_{f\,11} & K_{f\,12} \\ K_{f\,12} & K_{f\,22} \end{pmatrix}$. When the fracture permeability tensor is locally aligned with the fracture tangential and normal axes, this is written as $\boldsymbol{K_f} = \begin{pmatrix} K_{f,t} & 0.0 \\ 0.0 & K_{f,n} \end{pmatrix}$. Usually, the local cubic law (LCL) is used i.e. the diagonal tensor with $K_{f,t} \leq a_h^2/12$ which is the maximum tangential permeability of the region, of width a_h, representing flow between two parallel plates without tortuosity or cementation.

Tracer transport equation

The mass conservation equation for tracer transport ignoring dispersion is written as the advection equation below:

$$\varphi \frac{\partial c}{\partial t} + \nabla \cdot (\boldsymbol{v}c) = q_c \tag{2}$$

where, c is the tracer concentration and φ is the porosity which can be taken as unity here for simplicity.

3. CVD-MPFA Formulation Overview

The CVD-MPFA formulation overcomes the deficiency of standard reservoir simulation finite-volume methods which depend on a two-point flux approximation (TPFA) and are only consistent if the grid is K-orthogonal [32, 35]. The CVD-MPFA formulation depends on a single degree of freedom per control-volume, maintaining the optimal number of degrees of freedom as in standard reservoir simulation, and is comprised of families of flux-continuous locally-conservative finite-volume methods, that are consistent for full-tensor fields on general structured and unstructured grids. Cell-centred and cell-vertex CVD-MPFA formulations involve multiple families of schemes defined by the local flux quadrature point parameterization on each control-volume face [41]. Cell centred methods are considered here and a single family is parameterized by a dimensionless variable q. There are two basic types of CVD-MPFA formulation determined by the choice of basis functions: a) Triangle Pressure Support (TPS) with linear basis functions over subcell triangles leading to pointwise pressure continuity on control-volume sub-faces [35, 36]. b) Full Pressure Support (FPS) with subcell bilinear basis functions, leading to full pressure continuity over control-volume sub-faces [40–42]. In the cell-centred CVD-MPFA method, primal cells act as control-volumes, which are assigned rock properties, and discrete pressures are located at the primal cell centres as illustrated by the bold nodes numbered $1, 2, 3$ in Fig. 1a. Following the finite-volume method procedure, the first step is to integrate the flow equation (1) over each control-volume and apply the Gauss divergence theorem to obtain:

$$-\oint_{\delta\Omega_i} (\boldsymbol{K}\nabla\phi) \cdot \boldsymbol{n} dS = \int_{\Omega_i} q_c \, dV \tag{3}$$

where, $\delta\Omega_i$ denotes the boundary of an arbitrary control-volume Ω_i and $\boldsymbol{n}$ is a normal vector at the boundary $\delta\Omega_i$. The discrete scheme of Eq. (3) for CVD-MPFA is written as:

$$\sum_{k=1}^{2N_e} F_k = \bar{q}_c \tag{4}$$

4

(a) Cluster of triangular cells common to vertex V. Dual-cell is illustrated by the dotted line polygon

(b) Triangular pressure supports for sub-cells of cells 1 and 2 illustrated by filled blue triangles.

(c) Full pressure support for sub-cells of cells 1 and 2 illustrated by filled blue quadrilaterals.

(d) FPS fluxes are illustrated for sub-cells of cells 1 and 2. Points of flux computation are chosen by quadratures q_1 and q_2 for right and left sub-interfaces respectively, of the sub-cell

(e) Auxiliary dual-cell is illustrated by dashed polygon for full pressure support scheme
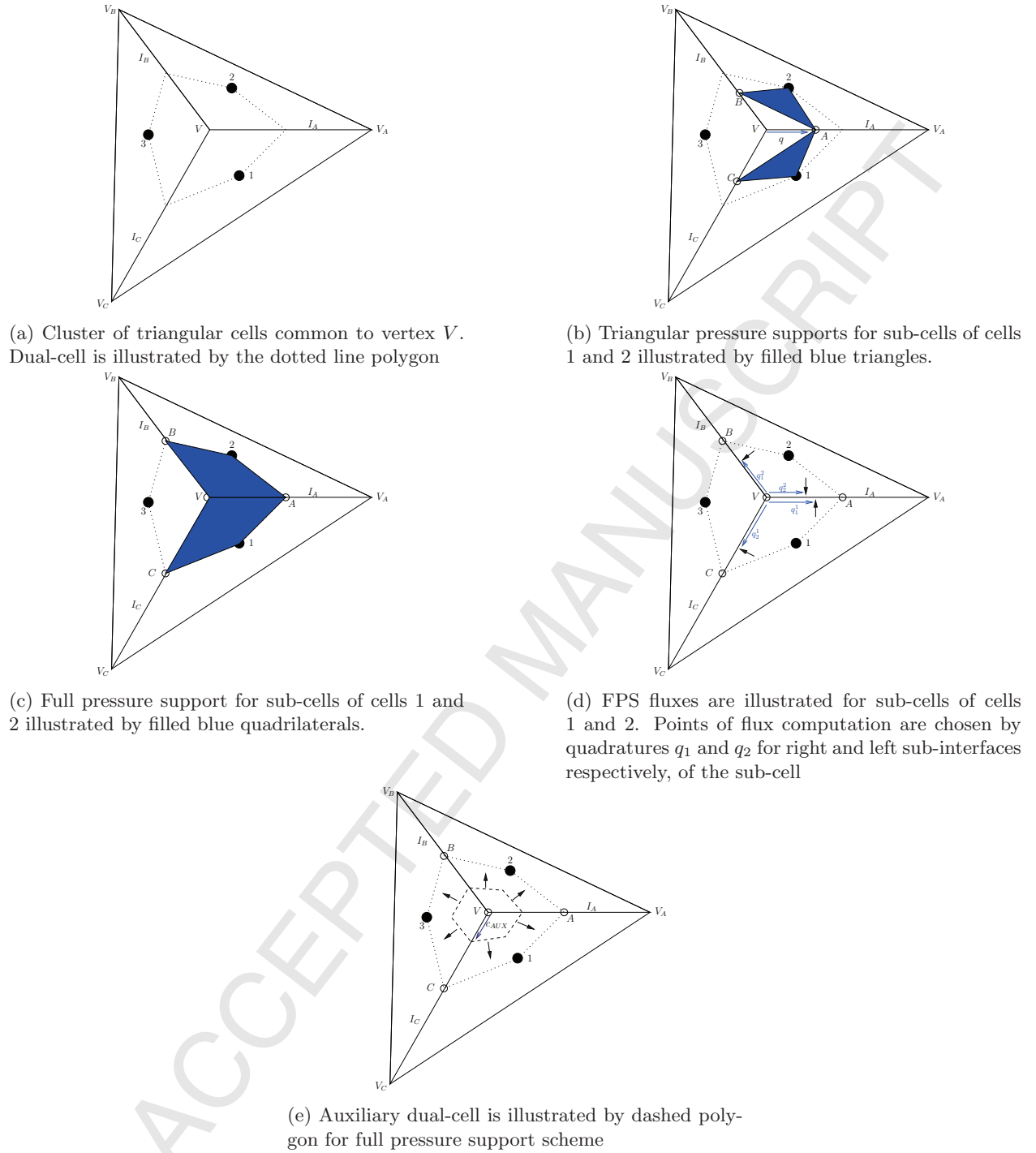
Figure 1: Cluster and dual-cell of three triangular cells.

95   where, F_k is the flux over one half of an edge (sub-interface) of a cell with N_e number of edges and $\bar{q}_c = \int_{\Omega_i} q_c \, dV$. Now we discuss the CVD-MPFA procedure to determine the fluxes on the edges of a cell.

Flux approximations are built using continuous flux and pressure constraints which are imposed locally with respect to each *cluster* of cells that are attached to a common grid vertex. A *dual-cell* is introduced which is

5

defined by connecting grid points (cell-centres) of cells with the mid-points of the edges which are attached
to the cluster vertex. The resulting polygon around the cluster vertex is called a dual-cell. A *sub-cell* is the
quadrilateral formed when dual-cells overlay the primal cell. Each sub-cell is defined by the anticlockwise
loop starting from the grid point (centroid) of a cell, then to the right-edge midpoint, cluster vertex, left-edge
midpoint, then back to the cell centroid. The edge mid-point divides the cell interface into two segments;
referred to as a *sub-interface*. In the CVD-MPFA method, normal flux continuity and pressure continuity
are fulfilled for every sub-interface. A cluster and dual-cell are shown in Fig. 1a.

3.1. Triangular pressure support (TPS) scheme

In the triangular pressure support (TPS) scheme, an auxiliary interface pressure is introduced on each
sub-interface to ensure point-wise pressure continuity. For a given dual-cell, the position of continuity can
be chosen at any point between the edge mid-point and the common grid vertex (but not at the (singular)
vertex) of the cluster of cells [36]. The continuity point is defined by the parametric variation in $[0 < q \leq 1]$
along the sub-interface, which leads to the family of schemes depending on the choice of quadrature q. The
singular point $q = 0$ corresponds to the cluster vertex (which is avoided) and $q = 1$ corresponds to the edge
midpoint and is the standard default method. In this work, a symmetric positive definite scheme is used with
$q = 2/3$ [36]. In this scheme, pressure is assumed piecewise linear over subcell triangles, an example triangle
is defined by joining the cell centre with the right-edge interface continuity point and left-edge interface
continuity point Fig. 1b, where pressure in the triangle of cell 1 is written in terms of barycentric coordinates
(ξ, η) where

$$\phi = (1 - \xi - \eta)\phi_1 + \xi\phi_A + \eta\phi_C \tag{5}$$

A piecewise constant pressure gradient vector is formed over each sub-cell from the pressure field, from which
the Darcy velocity vector can be determined in each sub-cell. The Darcy velocity is resolved along the two
outward sub-interface normals of the sub-cell. The normal flux at the left hand side of sub-interface I_A is
obtained by velocity resolution along the normal vector $\boldsymbol{dL_h} = 0.5((y_V - y_{V_A}), -(x_V - x_{V_A}))$ outward to
cell 1 where,

$$F_{I_A}^1 = \boldsymbol{v_h} \cdot \boldsymbol{dL_h} = -(T_{11}^1 \phi_\xi + T_{12}^1 \phi_\eta)|_A^1 \tag{6}$$

where, $\boldsymbol{T} = \boldsymbol{T}(q)$ is an approximation of the general Piola tensor (in physical space) and defines the co-
efficients of $(\phi_\xi, \phi_\eta)^{tr}$. For the full definition of the general tensor we refer to [36]. Similarly, fluxes are
determined on other sub-interfaces as well. Flux continuity is imposed on every sub-interface e.g, for I_A flux
continuity is written as,

$$
\begin{aligned}
F_{I_A}^1 &= -F_{I_A}^2 \\
-(T_{11}^1 \phi_\xi + T_{12}^1 \phi_\eta)|_{I_A}^1 &= (T_{21}^2 \phi_\xi + T_{22}^2 \phi_\eta)|_{I_A}^2
\end{aligned}
\tag{7}
$$

6

A system of flux continuity conditions results for each cluster. For the cluster of Fig. 1b flux continuity conditions are written in matrix form as

$$\boldsymbol{F} = \boldsymbol{A}_L^{3\times3}\Phi_m + \boldsymbol{B}_L^{3\times3}\Phi_I = \boldsymbol{A}_R^{3\times3}\Phi_m + \boldsymbol{B}_R^{3\times3}\Phi_I \tag{8}$$

where $\Phi_m = (\phi_1, \phi_2, \phi_3)^{tr}$ and $\Phi_I = (\phi_A, \phi_B, \phi_C)^{tr}$. Using condition (8), Φ_I is eliminated to yield the fluxes in terms of Φ_m written as,

$$\boldsymbol{F} = (\boldsymbol{A}_L + \boldsymbol{B}_L(\boldsymbol{B}_R - \boldsymbol{B}_L)^{-1}(\boldsymbol{A}_L - \boldsymbol{A}_R))\Phi_m \tag{9}$$

In this way, fluxes are determined on all the sub-interfaces related to a given cell in terms of primal grid-cell pressures only. The discrete scheme of Eq. (3) is then defined by the summation of assembled fluxes on all sub-interfaces of the triangular control-volumes.

3.2. Full pressure support (FPS) scheme

The full pressure support scheme retains sub-interface pressures at the midpoint of the primal interfaces together with an additional auxiliary pressure introduced at the vertex of the cluster, which gives rise to full pressure continuity along each sub-interface in the cluster [42]. A piecewise bilinear pressure approximation is defined over each sub-cell by connecting the four corner pressures, which involve one primal cell-centred pressure, two sub-interface pressures at the midpoints of the corresponding primal interfaces and the auxiliary pressure at the vertex of the cluster. Referring to Fig. 1c, the bilinear pressure over the illustrated sub-cell of cell 1 is given by

$$\phi = (1-\xi)(1-\eta)\phi_1 + \xi(1-\eta)\phi_A + \xi\eta\phi_V + (1-\xi)\eta\phi_C \tag{10}$$

The Darcy velocity vector is determined in each sub-cell from the pressure field and is resolved along the normal to each of the sub-interfaces. The Flux for cell 1 on the sub-interface I_A is then expressed in the form of expression (6). Here, the flux is expressed in terms of the (auxiliary) interface pressures and the additional auxiliary vertex pressure. The definition of the general tensor for FPS is given in [42]. For FPS, the tensor $\boldsymbol{T} = \boldsymbol{T}(q_1, q_2)$ depends on the two quadratures $0 < q_1 \leq 1$ and $0 < q_2 \leq 1$ which define the points of the flux computation on the right sub-interface and left sub-interface respectively of the sub-cell. Consequently each sub-cell can have its own multi-family quadrature values. $q_1 = 0$ corresponds to the point on the common vertex of the cluster and is avoided, while $q_1 = 1$ corresponds to the midpoint of the primal interface and is the default quadrature value, q_2 has a similar definition. Referring to the Fig. 1d, q_1^1 and q_2^1 are the quadratures for sub-cell of cell 1 on the interfaces I_A and I_C. Similarly, q_1^2 and q_2^2 are the quadratures for sub-cell of cell 2 on the interfaces I_B and I_A. Here we use a single family quadrature value with $q = q_1 = q_2$ for the computations. Fluxes are defined on both sides of each sub-interface and imposed to be continuous as expressed in Eq. (7) for the interface I_A, analogous to the TPS formulation. Continuity of fluxes on the sub-interfaces are used to eliminate the pressures at the midpoints of the primal interfaces. To eliminate

7

the auxiliary pressure at the vertex an additional equation is needed. For this purpose, the divergence free condition of the partial differential equation over an auxiliary dual-cell is utilized (Fig. 1e) written as $-\oint_{\partial\tilde{\Omega}_{i_{AUX}}}(\boldsymbol{T}\tilde{\nabla}\phi)\cdot\boldsymbol{n}dS = 0$ for the auxiliary control-volume $\tilde{\Omega}_{i_{AUX}}$ in the auxiliary dual-cell surrounding the vertex of the cluster. The size of the auxiliary dual-cell is controlled by the parameter $0 < c_{AUX} \leq 1$, where

160   $c_{AUX} = 1$ corresponds to the size which matches the actual dual-cell. A very small value (10^{-5}) of c_{AUX} is optimum for the computations [42]. The flux continuity conditions and the divergence free condition are written, for the cluster shown in Fig. 1c, are combined in the form;

$$\boldsymbol{F} = \boldsymbol{A}_L^{4\times3}\Phi_m + \boldsymbol{B}_L^{4\times4}\Phi_I = \boldsymbol{A}_R^{4\times3}\Phi_m + \boldsymbol{B}_R^{4\times4}\Phi_I \tag{11}$$

where $\Phi_m = (\phi_1, \phi_2, \phi_3)^{tr}$ and $\Phi_I = (\phi_A, \phi_B, \phi_C, \phi_V)^{tr}$. Using condition (11), we can eliminate Φ_I to obtain the fluxes in terms of Φ_m expressed in an analogous form to Eq. (9).

165   The motivation for extending the FPS formulation to discrete fracture-matrix modelling is the robustness of the FPS formulation, which is illustrated in the results section by comparisons with the TPS formulation. The TPS formulation can yield results with strong spurious oscillations for challenging test cases involving strongly anisotropic full-tensor fields, with e.g. injector/producer wells (or source/sinks) present. In contrast FPS methods overcome the TPS limitation and yield well resolved pressure fields that are free of strong

170   spurious oscillations [40–42], where M-matrix conditions are also presented. While both the TPS and FPS formulations are shown to violate M-matrix conditions in such cases (i.e. for full-tensor fields where TPS induces oscillations) and therefore lack a discrete maximum principle, it is also shown that the TPS formulation permits decoupled solution modes for such cases, and conversely that the FPS formulation prevents such modes and thus prevents their accompanying spurious oscillations at grid resolution level, allowing the

175   full multi-family quadrature range for flux approximation [40–42].

4. Hybrid-grid CVD-MPFA for fractured media

The simplest and the most straightforward modelling of a discrete-fracture matrix system is achieved by using the equi-dimensional model where thin fractures are gridded by small grid cells and are assigned fracture permeability. The numerical method (e.g. CVD-MPFA) is employed to solve the problem on a

180   given mesh just as in the case of a heterogeneous medium. Because of the small apertures of fractures, grid generation is complicated and numerical simulation is costly, specifically in the case of intersecting fractures. The intermediate cells between the intersecting fractures have dimensions of fracture aperture which increases the condition number of the global linear system and reduces the time-step size limit for transport problems when using an explicit method, thus increasing the overall computational cost. To address

185   the problems associated with equi-dimensional fracture modelling, the hybrid-grid method was introduced for the cell-centred finite-volume method with a two-point flux approximation (TPFA) for the discrete-fracture model [47]. The TPFA scheme has an O(1) error when the grid is not K-orthogonal. Sandve

et. al. [31] presented a hybrid-grid method using the multi-point flux approximation, (equivalently TPS with default $q = 1$), for single-phase fluid flow simulations in a fractured porous medium. In the hybrid-grid method, fractures are modelled by lower-dimensional entities in the geometric mesh but are expanded to equi-dimensional cells in the computational domain. In 2D, the mesh is conforming with fractures on cell edges, which are expanded to rectangular cells in the computational domain leading to a hybrid-mesh. The main difference between the hybrid-grid method and the equi-dimensional method is in the treatment of adjusted geometry and intermediate cells. In [31], computations are performed without adjusting the actual area of the neighbouring matrix cells when fracture cells are expanded from the physical mesh to the computational domain. In the hybrid-grid, unknowns are associated with the centroids of matrix cells and lower-dimensional fracture cells. During computations the fracture is given an area which is equal to the length of the edge between matrix cells, multiplied by the aperture of the fracture. The hybrid cells are represented by insertion of midpoints on the edges of the fracture cell, which are a half-aperture away on both sides of the fracture centroid. When compared to the equi-dimensional method, in the hybrid-grid method, intermediate cells at the intersection of fracture cells are assumed to be so small that pressure variation is zero and pressure associated with intermediate cells is eliminated locally, thus reducing the global degrees of freedom and also the computational cost.

The CVD-MPFA formulation determines the fluxes locally over each dual-cell. We present the local hybrid-grid formation and the respective dual-cell formulation in the following sub-section. We then review the TPS scheme for hybrid-grids followed by the more robust *full pressure support* (FPS) scheme, formulated using the new hybrid-grid for fractured porous media.
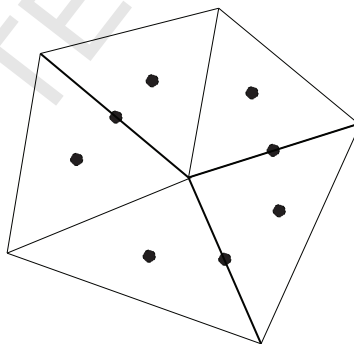

Figure 2: Cluster involving fracture edges, depicted by bold edges. The centroids of the cells are also shown.

4.1. Hybrid-grid formation

Here, we present a consistent and novel hybrid grid formation, generated locally with respect to a dual-cell, involving fracture cells and applies to fractures of general shape trajectory and allows for intersection. We form the hybrid-grid within the concerned dual-cell, adjusting the geometry of the neighbouring sub-cells to maintain consistent approximation of fluxes on sub-interfaces, while circumventing conventional equi-dimensional mesh generation issues that arise when using the equi-dimensional model.
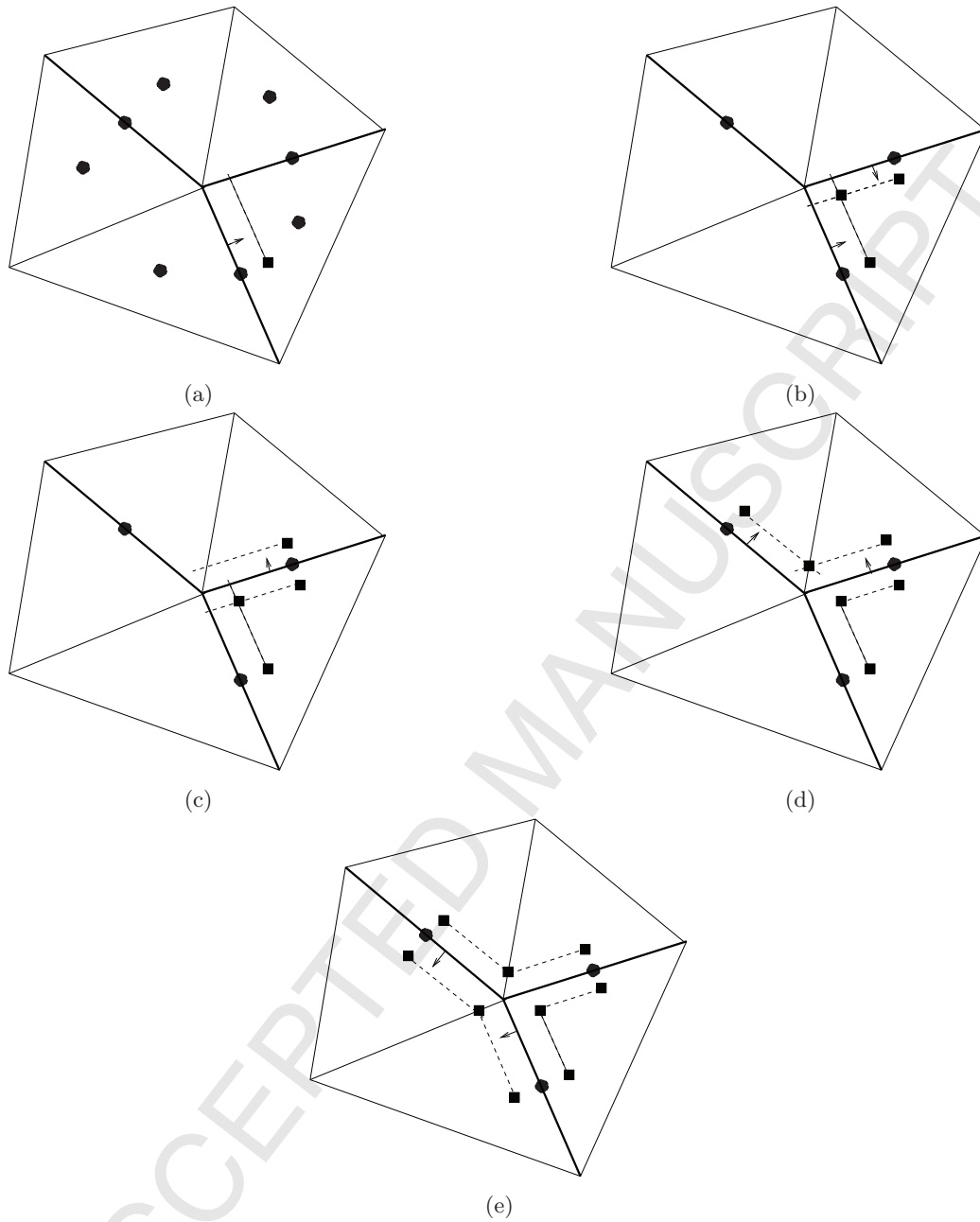
9

Figure 3: Process of hybrid sub-cells formation. "Squares" depict the new geometry points inserted and "dots" are the primal centroids of the physical cells. (a)-(e) are the steps of the determination of consistent hybrid-faces and hybrid sub-cells. Dashed lines are the new hybrid half-faces.

Consider a cluster of five matrix cells and three fracture cells, represented by edges in between the 2D matrix cells, in Fig. 2. The process of formation of the hybrid-grid for the concerned cluster of cells is also represented in Fig. 3. We start using any edge common to the vertex of the cluster, and loop through all N_{De} edges of the cluster in anticlockwise fashion.

For edges $1 : N_{De}$

- Step 1: Check if the edge is a fracture cell. If the edge is a fracture cell go to the next step otherwise
₂₂₀ move to the next edge in the anticlockwise direction.

- Step 2: Compute the edge midpoint. Project the midpoint and dual vertex in an anticlockwise normal direction to a distance of a half-aperture to define a ghost line. Go to next step.

- Step 3: Find the next edge, in the anticlockwise loop, which is a fracture cell. Compute the midpoint, project the midpoint and dual-vertex in clockwise normal direction to a distance of half-aperture to
₂₂₅ make another ghost line. Go to the next step.

- Step 4: Find an intersecting point of the two ghost lines. Store the new point, in the database, as the new vertex for all the matrix cells in between the concerned fracture cells. Store the new midpoints as well. Move to next edge in loop and go to Step 1.

The above process, yields the modified sub-cells for the matrix cells and the fracture cells which are defined
₂₃₀ by newly added points depicted by squares in Fig. 3. Physical areas of the modified sub-cells are computed and added to the corresponding global cell areas. The centroids of the cells are unchanged and are the centroids of the original cells in the mesh.

The final sub-cells and the dual-cell for computations with the TPS scheme are shown in Fig. 4a. We reiterate here that this process is local to the dual-cell for flux approximation, without changing the whole physical mesh. By the above process, flux approximation on hybrid grids is consistent.
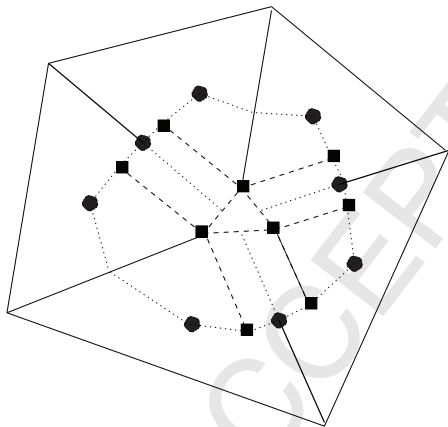
(a) The hybrid dual-cell for the cluster (Fig. 2) for TPS formulation
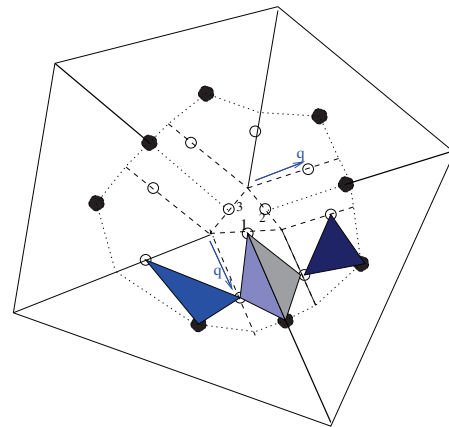
(b) Triangular pressure support is illustrated for a hybrid-grid. Pressure points on the interfaces and hybrid faces are depicted by circles and primal pressures are depicted by dots

Figure 4: Dual cell and hybrid sub-cells for TPS.

₂₃₅

4.2. Hybrid-grid TPS

The CVD-MPFA triangular pressure support (TPS) scheme is now applied to the set of modified sub-cells that are obtained by the above process. Pressure points on the edges between matrix-matrix cells

11

and matrix-fracture faces are eliminated by imposing continuity of flux on each edge. Continuity of fluxes

240 is imposed at the matrix-matrix and matrix-fracture sub-interface pressure points, to eliminate interface

pressures on the sub-interfaces. To eliminate pressures on the hybrid faces of an intermediate cell between

intersecting fractures, two conditions are imposed. First, pressures on all hybrid faces of an intermediate

cell are continuous and second, summation of fluxes on these faces is zero. For a dashed-line triangular

intermediate cell of the cluster shown in Fig. 4b, the conditions can be written as:

245 $\phi_k = \phi_v \quad k = 1, 2, 3 \qquad$ and $\qquad \sum_{k=1}^{3} F_k = 0$

Note that, the condition of zero accumulation of mass in the small cell at intersection ($\sum_{k=1}^{l} F_k c_k = c_{fo} \sum_{k=1}^{3-l} F_k$)

is also used for transport solutions, to avoid the local cell CFL condition cf. [31].

The flux continuity conditions and the divergence condition over the intermediate cell are written in a

combined form for the cluster shown in Fig. 4b as:

$$A_L^{9\times8}\Phi_c + B_L^{9\times9}\Phi_I = A_R^{9\times8}\Phi_c + B_R^{9\times9}\Phi_I \tag{12}$$

250 where, Φ_c is a vector of pressures associated with the cell centres (5 matrix and 3 fracture cells) and Φ_I is

a vector of interface pressures associated with the sub-interfaces and the intermediate cell (8 sub-interfaces

and an intermediate cell). Eliminating Φ_I, by the flux continuity conditions and the divergence condition

over the intermediate cell, we obtain all the fluxes (8 on sub-interfaces and 3 on hybrid-faces of intermediate

cell) required for the matrix and fracture cells in terms of only the cell-centred pressures with:

$$F = (\bar{A}_L^{11\times8} + \bar{B}_L^{11\times9}(B_R^{9\times9} - B_L^{9\times9})^{-1}(A_L^{9\times8} - A_R^{9\times8}))\Phi_c \tag{13}$$

255 Consequently, after assembly, the finite-volume approximation yields a linear system of equations with so-

lution vector comprised of a global cell-centred pressure field. This process leads to consistent flux approx-

imation on hybrid grids, which is equi-dimensional with the exception of intersecting fracture cells, which

are treated by the special local approximation described above.

4.3. Hybrid-grid FPS

260 The CVD-MPFA full pressure support (FPS) scheme (which is reviewed in the previous section) has

proven to be robust with improved convergence behaviour for both pressure and velocity, when compared

to the point-wise continuous TPS scheme. In particular, for very highly anisotropic strong full-tensor per-

meability fields, cell-centred TPS violates the M-matrix conditions and induces spurious oscillations at grid

level due to decoupling, which are prevented by the FPS formulation [40, 42]. Here, we present the FPS

265 formulation for modelling fractured media with the hybrid-grid method.

As FPS has full pressure continuity along each sub-interface, achieved by using an additional vertex pressure,

we do not apply FPS on the hybrid dual-cell, shown in Fig. 4a, that is used for the hybrid-grid TPS method.

Instead we propose a new hybrid dual-cell by collapsing the intermediate cell and extending the fracture

12
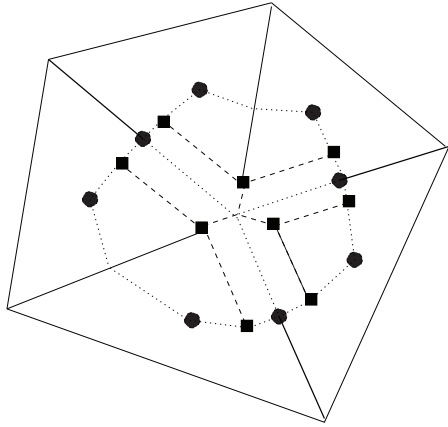
(a) The hybrid dual-cell for the cluster (Fig. 2) for FPS formulation
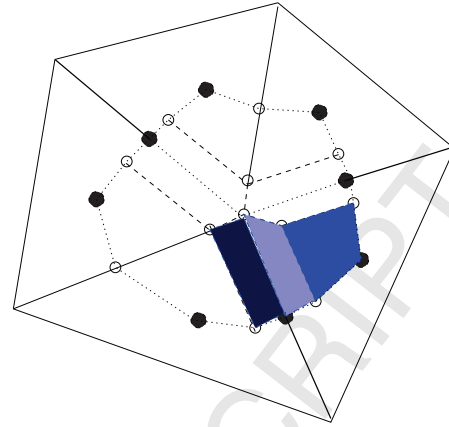
(b) Full pressure support for some of the cells are shown for hybrid-grid. Auxiliary pressure nodes on the interfaces, hybrid faces and vertices are depicted by hollow circles and primal pressures are depicted by full circles (dots)
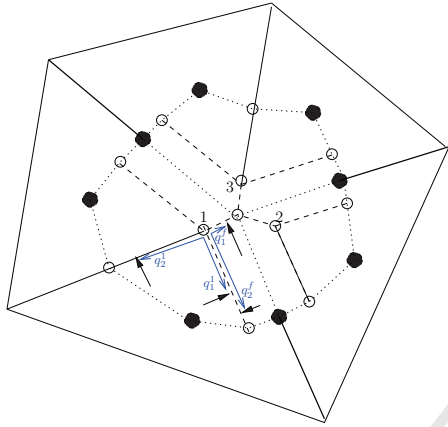
(c) Fluxes and quadratures are shown for a matrix and a fracture cell for FPS formulation
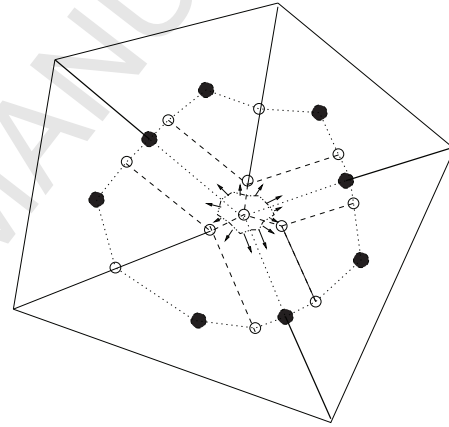
(d) Auxiliary dual-cell for the fracture cells is shown to eliminate the vertex pressure between fracture cells

Figure 5: Dual cell and hybrid sub-cells for FPS formulation.

cells. The proposed hybrid dual-cell for FPS is shown in Fig. 5a. Pressure in each of the resulting sub-cells of

270 Fig. 5a has full pressure support, constructed by the pressures at the midpoint of interfaces, the vertices and the cell-centres. In this way, we have full pressure continuity along the matrix-matrix, the matrix-fracture and the fracture-fracture sub-interfaces. Fluxes on the sub-interfaces of all the sub-cells are determined from the Darcy velocity for given quadrature values for the sub-cells. Full pressure support for some of the matrix and fracture cells of the dual-cell are shown in Fig. 5b. Fluxes on the sub-interfaces of a matrix sub-cell and

275 a fracture sub-cell are also shown in Fig. 5c. The quadrature ranges in a sub-cell of a primal matrix cell are defined by $0 < q_1^1 \leq 1$ and $0 < q_2^1 \leq 1$ on the right sub-interface and the left sub-interface, respectively, Fig. 5c. The quadrature ranges in a sub-cell of a fracture cell are defined by $0 < q_1^f < 1$ and $0 < q_2^f \leq 1$ on the right sub-interface and the left sub-interface, respectively, see Fig. 5c. Note that, $q_1^f = 1$ is excluded as the corresponding sub-interface is the fracture-fracture hybrid-face, see [42]. We determine the fluxes on

13

₂₈₀ both the sides of the sub-interfaces via resolving respective sub-cell Darcy velocities normal to the interface where each Darcy velocity is a function of the local sub-interface pressures, the vertex interface pressures and the cell-centred pressures.

For the cluster shown in Fig. 5b, we have 8 cell-centred pressures (5 matrix cells and 3 fracture cells), 8 (auxiliary) pressures on the sub-interfaces, 1 (auxiliary) pressure associated with the primal vertex between ₂₈₅ the fracture cells and three additional auxiliary vertex pressures which connect to the matrix as well as the fracture cells. The three additional vertex pressures are indicated by the numbered hollow circles in Fig. 5c. We impose flux continuity on the sub-interfaces between matrix-matrix cells and between the matrix and fracture cells to eliminate the pressures associated with the midpoints of the primal interfaces. We require four additional conditions to eliminate the auxiliary pressures at the junction primal vertex and the three ₂₉₀ additional vertices. For this purpose we impose the zero divergence condition over an auxiliary dual-cell surrounding the primal vertex joining the fracture cells, to eliminate the auxiliary vertex pressure, see Fig. 5d. In addition, we impose flux continuity on the interfaces (hybrid-faces) between the fracture cells to eliminate pressures associated with the three additional vertices (numbered hollow circles in Fig. 5c) thus avoiding $q_1^f = 1$ on the hybrid-face and the associated singularity. The divergence condition and eleven continuity ₂₉₅ conditions for cluster shown in Fig. 5b are written in the form:

$$\boldsymbol{A}_L^{12\times8}\Phi_c + \boldsymbol{B}_L^{12\times12}\Phi_I = \boldsymbol{A}_R^{12\times8}\Phi_c + \boldsymbol{B}_R^{12\times12}\Phi_I \tag{14}$$

where, Φ_c is the vector of cell-centred pressures (5 matrix and 3 fracture cells) and Φ_I is the vector of auxiliary pressures associated with the 8 sub-interfaces and 4 vertices. Eliminating Φ_I, fluxes on all sub-interfaces involved in the cluster are expressed in terms of primal cell-centred pressures as:

$$\boldsymbol{F} = (\bar{\boldsymbol{A}}_L^{11\times8} + \bar{\boldsymbol{B}}_L^{11\times12}(\boldsymbol{B}_R^{12\times12} - \boldsymbol{B}_L^{12\times12})^{-1}(\boldsymbol{A}_L^{12\times8} - \boldsymbol{A}_R^{12\times8}))\Phi_c \tag{15}$$

The procedure leads to consistent flux approximation with full pressure continuity on hybrid grids. After ₃₀₀ assembly of the fluxes the resulting finite-volume approximation yields a linear system of equations for the global cell-centred pressures.

In this work, we present a description of the method in 2D. The above method can be extended to 3D but involves further complexities because of the additional dimension. Pressure variation is defined by a tri-linear variation in each hexahedral sub-cell of a grid-cell. FPS involves a higher number of local degrees of freedom ₃₀₅ in a dual-cell compared to 2D, which enables the scheme to apply to full-tensor permeability fields in 3D. Construction of a general polyhedral dual-cell that arises in the hybrid-grid method involving various cases of intersecting fractures is complex and challenging in 3D. We will present details of the 3D method in future work.

14

5. Numerical results

We present numerical results in this section, to assess the performance of the FPS scheme applied to a fractured porous medium. We start with the convergence behaviour of the FPS scheme for a domain with a single fracture. In the subsequent sub-sections, we compare transport results obtained by the hybrid-grid TPS scheme and the FPS scheme with the results obtained using refined 2D fractures for single and intersecting fractures with diagonal isotropic and anisotropic full-tensor permeability fields. We also present results for a fractured domain with zigzag discontinuous and anisotropic full-tensor permeability field. Furthermore, we compare the condition number of the linear systems obtained by the hybrid-grid FPS and the 2D gridded fracture method. A transient pressure simulation of compressible gas flow is also presented for a complex discrete fracture-matrix system.
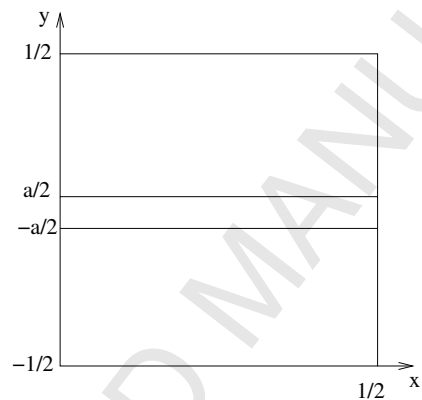

Figure 6: Case 1: Square domain with single fracture in the middle

5.1. Case 1: Convergence test

We perform convergence tests for both the hybrid methods with TPS and FPS for a domain with a single fracture as used in [20, 31]. Fig. 6 shows a domain with a single fracture of aperture a. Permeability of the domain is isotropic with that of the fracture being a constant multiple of the matrix.

$$\boldsymbol{K}(x,y) = \begin{cases} \boldsymbol{K}_m(x,y) & (x,y) \in \Omega_m \\ k_f \boldsymbol{K}_m(x,y) & (x,y) \in \Omega_f \end{cases}$$

where, $\boldsymbol{K}_m = \begin{pmatrix} 1 & 0 \\ 0 & 1 \end{pmatrix}$ mD and k_f is the permeability ratio of the fracture to that of the matrix. Exact pressure for the domain (Fig. 6) can be calculated analytically, and is given by:

$$\phi(x,y) = \begin{cases} k_f cos(x)cosh(y) + (1 - k_f)cos(x)cosh(a/2) & (x,y) \in \Omega_m \\ cos(x)cosh(y) & (x,y) \in \Omega_f \end{cases}$$

15

for the source:

$$q_c(x,y) = \begin{cases} (1 - k_f)cos(x)cosh(a/2) & (x,y) \in \Omega_m \\ 0 & (x,y) \in \Omega_f \end{cases}$$

Dirichlet boundary conditions are imposed on all the external boundaries of the domain. We discretise the domain into $N \times N$ regular quadrilateral elements where the fracture is initially represented by interfaces between the elements. We compute normalised error norms for pressure as defined in [31]. In Fig. 7,
330 normalised error norms of pressure are plotted against aperture to cell length ratio a/L_h for a series of $N \times N$ elements where $N = 10, 20, ..., 100$. For comparison, we show convergence plots of the hybrid-grid TPS method (continuous lines) and hybrid-grid FPS method (broken lines), for different values of aperture a and permeability contrast k_f. As shown in Fig. 7, the L^2 errors of the hybrid-grid TPS and the hybrid-grid
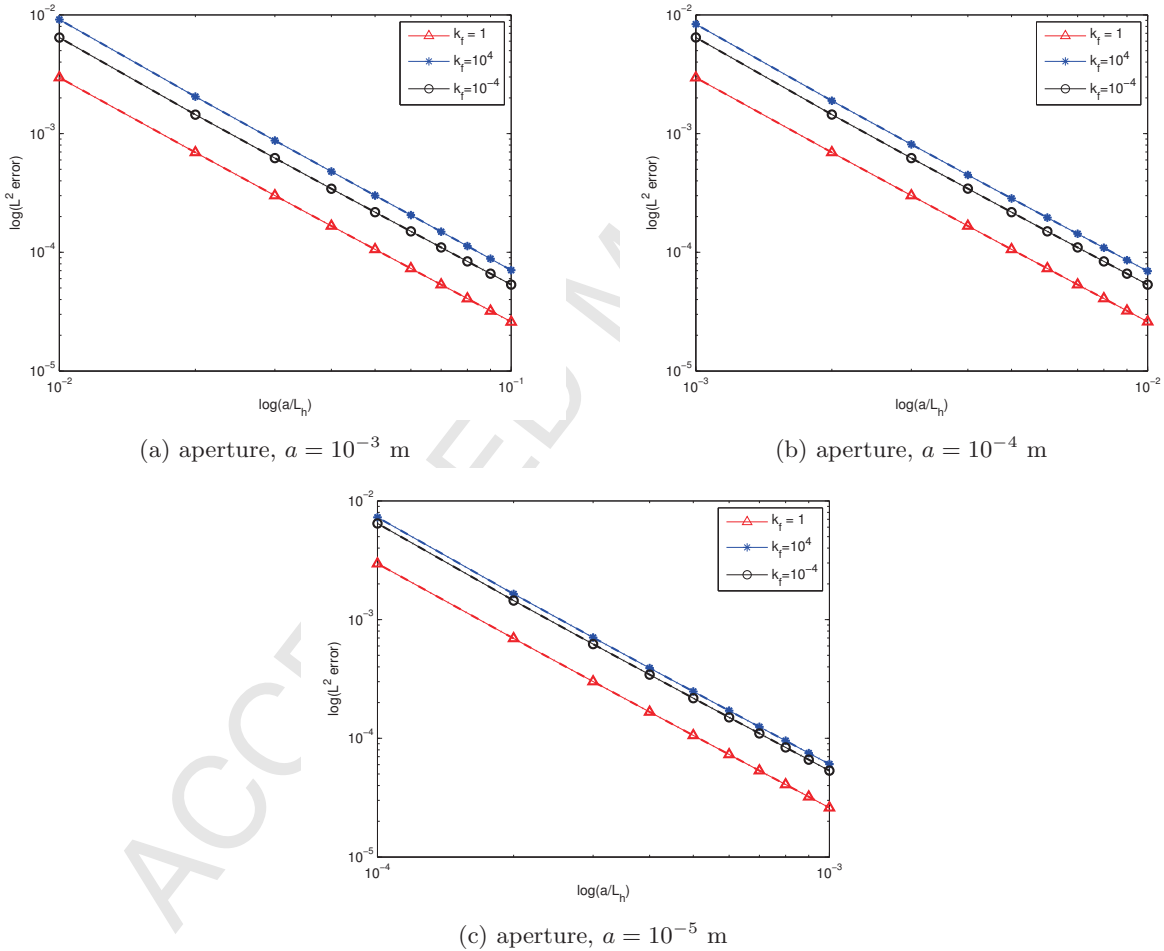

(a) aperture, $a = 10^{-3}$ m

(b) aperture, $a = 10^{-4}$ m

(c) aperture, $a = 10^{-5}$ m

Figure 7: Case 1: Normalised error vs a/L_h for different aperture values and for different permeability contrast ratios k_f. L_h is the cell length of the Cartesian grid. Continuous lines show convergence for the hybrid-grid TPS method while broken lines show convergence of the hybrid-grid FPS method. Plots of TPS and FPS overlap each other for each of the values of k_f.

FPS are almost identical to each other. L^2 errors of the hybrid-grid FPS method are similar to the errors
335 of the hybrid-grid TPS for all the cases with homogeneous permeability ($k_f = 1.0$) as well as heterogeneous permeabilities where the fracture has higher ($k_f = 10^4$) and lower ($k_f = 10^{-4}$) permeabilities compared

16

to the permeability of the matrix. Convergence of the hybrid-methods is the same for all the values of aperture considered. Note that the convergence of the hybrid-grid methods discussed here is comparable to the convergence of the equi-dimensional method [31, 33] (for this single fracture problem) in contrast to the convergence results shown for hybrid-grid TPS method in [31] and for the TPS coupled with a lower-dimensional fracture model [33]. Plots for the hybrid-grid TPS method in [31] show divergence away from the straight plots of the equi-dimensional method for $k_f = 1$ and $k_f = 10^4$ when $a = 10^{-3}$ and $a = 10^{-4}$. The improvement in the hybrid-grid method shown here, when compared to [31], is primarily attributed to the newly introduced consistent hybrid-grid formation, locally in the dual-cell.

5.2. Case 2: Comparison of transport solution with reference solution

In this section, we compare the transport solutions obtained by the hybrid-grid TPS and hybrid-grid FPS methods with the reference solutions. We solve problems on the refined mesh where the fractures are explicitly gridded by 2D triangular cells and the solutions define the reference in each case. A sequence of problems is considered: a problem of a domain with a single fracture, a problem with multiple intersecting fractures, and we consider both diagonal and full-tensor permeability fields. 2D fracture problems are solved using both CVD-MPFA TPS and FPS schemes, with default quadrature value of ($q = 1$). Grids used for the tests have been generated by using the Triangle [48] unstructured mesh generator.

5.3. Case 2a: Single fracture

We consider a domain with a single fracture along the diagonal of the square domain. The aperture of the fracture is $a = 1$ mm and the ratio of the fracture permeability to the matrix permeability is $k_f = 10^4$. Length and height of the domain is $L_x = L_y = 1$ m. The meshes are shown in Fig. 8. We consider two different cases of permeability fields. For both the cases, zero-flux Neumann boundary conditions are imposed on the whole external boundary of the domain. Fluid is injected through an injector I with rate 0.3114 pore volumes (PV) per year and pressure $\phi = 0$ bar is specified at the diagonally opposite producer. Concentration of the tracer is determined by solving the transport equation for each time step, using the first order upwind scheme.

1. *Diagonal tensor field:* First of all, we consider a diagonal isotropic permeability tensor in the whole domain. The fracture has a higher permeability increased by a factor k_f multiplying the permeability of the matrix i.e. $\boldsymbol{K_m} = \left(\begin{smallmatrix} 1.0 & 0.0 \\ 0.0 & 1.0 \end{smallmatrix} \right)$ mD and $\boldsymbol{K_f} = k_f \times \boldsymbol{K_m}$. Pressure plots obtained by the CVD-MPFA schemes on the reference mesh and the hybrid-grid are shown in Fig. 9. Contours of tracer concentration at the producer at pore-volumes-injected (PVI)= 0.9337 are shown in Fig. 10. Plots of tracer concentration at the producer for reference pressure solutions and pressure solutions computed by the hybrid-grid TPS and FPS methods are shown in Fig. 13a. Tracer concentrations resulting from the TPS and the FPS schemes, applied on the reference refined mesh, are very close to each other and plots overlay each other. Tracer plots for the hybrid-grid TPS and FPS are very close to each other and follow the behaviour of the reference solution.

17

(a) Reference mesh with explicit 2D fracture cells. No. of cells = 48225

(b) Mixed-dimensional mesh: 3096 2D matrix cells + 26 1D fracture cells

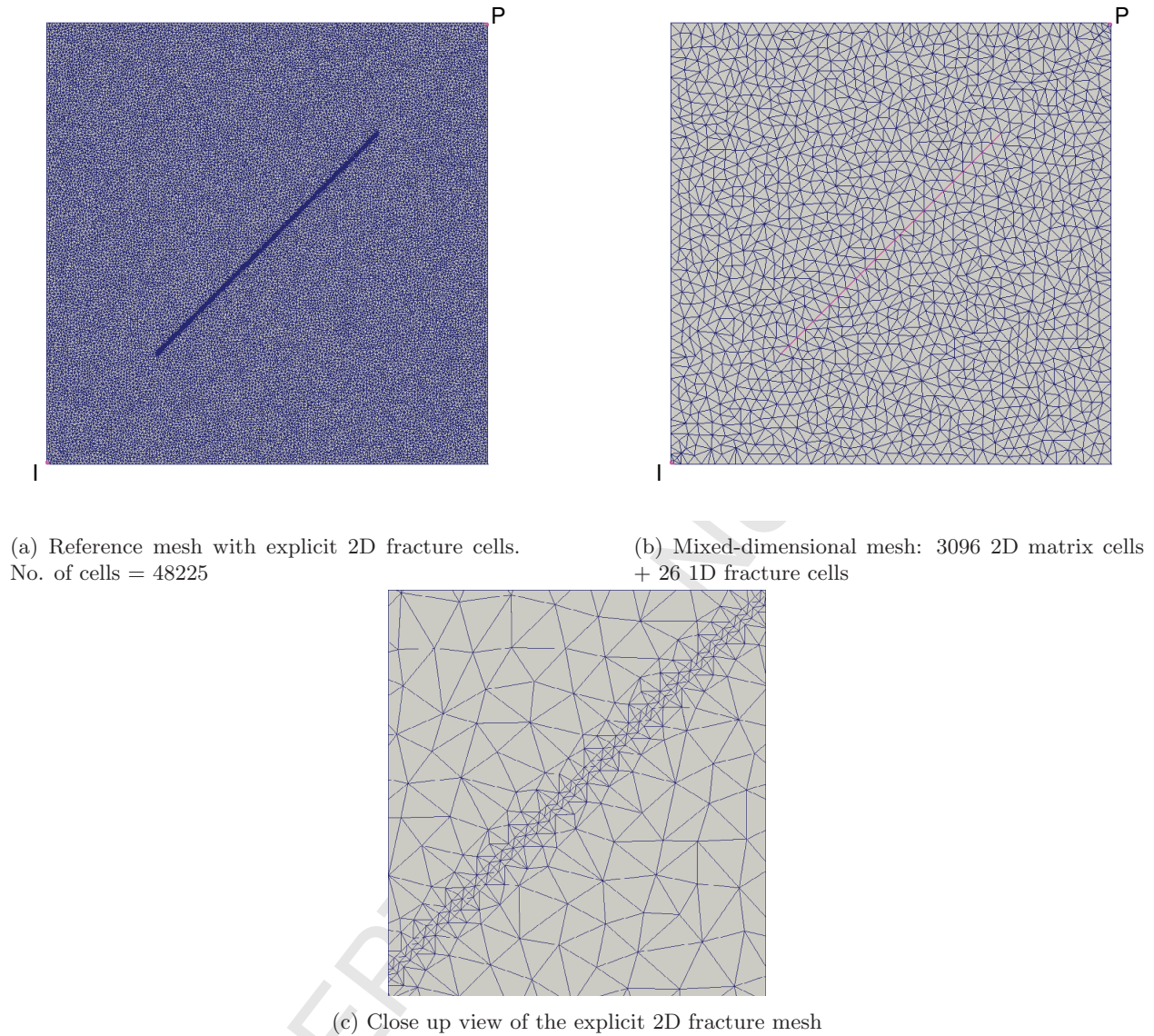(c) Close up view of the explicit 2D fracture mesh

Figure 8: Case 2a: (a) Explicit grid representation of fracture and (b) mixed-dimensional grid for domain with single fracture. Injector is marked by I and producer is marked by P.

2. *Full-tensor field:* Now, we consider a relatively weak anisotropic full permeability tensor $(10 : 1$ at an angle $30^o)$ in the whole domain. Matrix permeability tensor is defined by $\boldsymbol{K_m} = \left(\begin{smallmatrix} 0.7750 & 0.38971 \\ 0.38971 & 0.3250 \end{smallmatrix} \right)$ mD and the fracture permeability tensor is defined by $\boldsymbol{K_f} = k_f \times \boldsymbol{K_m}$. Pressure solutions are shown in
375   Fig. 11 and concentration contours are shown in Fig. 12. Some discrepancy is observed in the pressure solution of the hybrid-grid TPS method when compared to the reference solutions. Tracer concentration plots versus time are shown in Fig. 13b which show that hybrid-grid FPS yields more accurate tracer concentration values, clearly closer to the reference plots compared to the results obtained by the hybrid-grid TPS, indicating that FPS is beneficial compared to TPS for the relatively low anisotropy
380   ratio of $10 : 1$ at 30°.

18
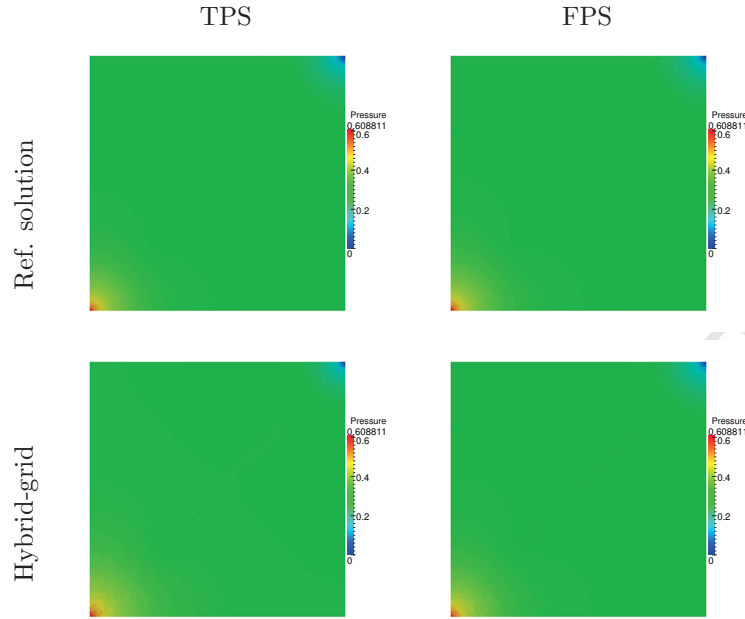
Figure 9: Case 2a: Reference pressure solutions by the TPS and FPS in first row and pressures computed by hybrid-grid TPS and FPS in second row for a diagonal isotropic field over a domain with a single fracture.
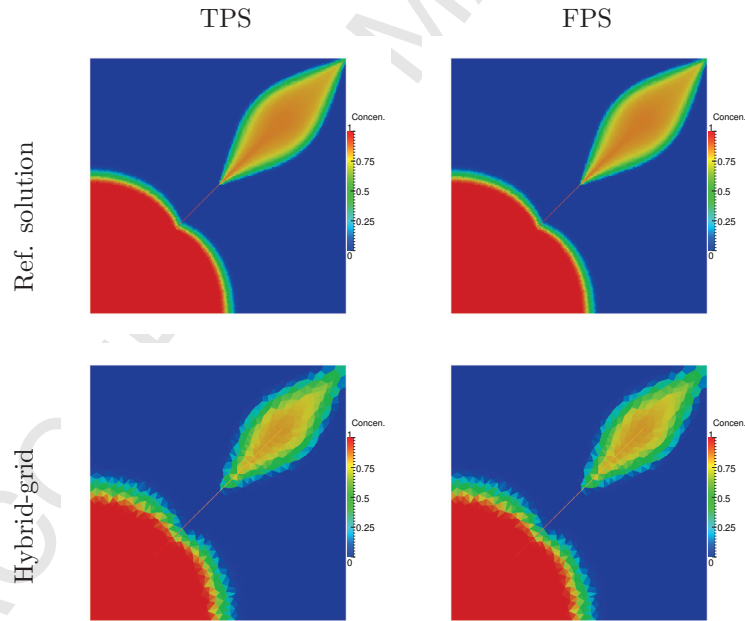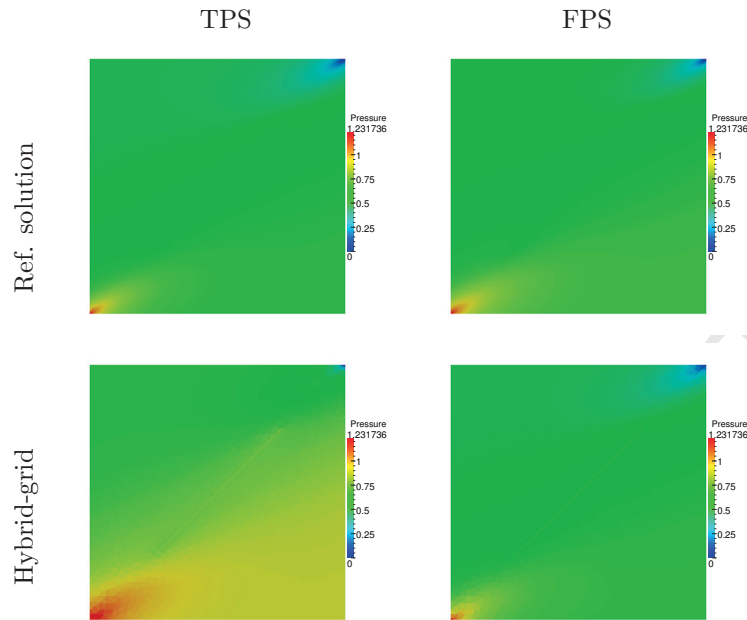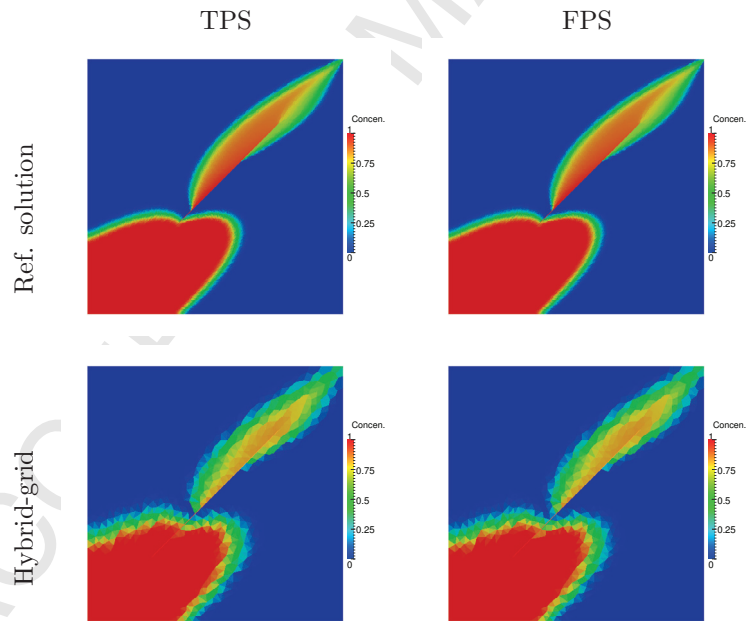

Figure 10: Case 2a: Tracer concentration contours at PVI= 0.9337 corresponding to the reference pressure solutions in first row and hybrid-grid TPS and FPS in second row for a diagonal isotropic field over a domain with a single fracture.

5.4. Case 2b: Multiple intersecting fractures

In this section, a domain with six intersecting fractures is considered. The aperture of the fractures is $a = 1$ mm and the fracture to matrix permeability ratio is $k_f = 10^6$. The dimensions of the domain is

19

Figure 11: Case 2a: Reference pressure solutions by TPS and FPS in first row and pressures computed by hybrid-grid TPS and FPS in second row for an anisotropic $(10 : 1$ at $30^o)$ field over a domain with a single fracture.

Figure 12: Case 2a: Tracer concentration contours at PVI= 0.9337 corresponding to the reference pressure solutions in first row and hybrid-grid TPS and FPS in second row for an anisotropic $(10 : 1$ at $30^o)$ full-tensor field over a domain with a single fracture.

1×1 m^2. A mesh for reference solution with explicit 2D gridded fractures and two mixed-dimensional meshes

385   (coarse and fine) for the hybrid-grid method are shown in Fig. 14. We show pressure solutions computed by

20

(a) Isotropic

(b) Anisotropic $10 : 1$ at 30°
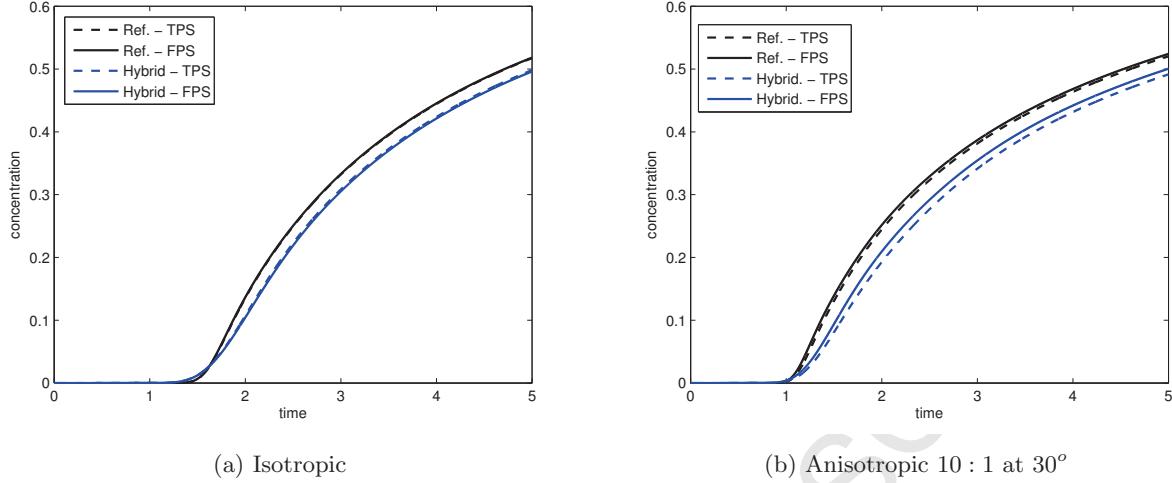
Figure 13: Case 2a: Tracer concentrations at producer versus time (years) for the reference pressure solutions by the TPS and FPS and hybrid-grid pressure solutions for the domain with a single fracture.

the hybrid-grid method for the coarse mesh shown in Fig. 14c. We consider three different permeability fields for this domain. Zero-flux boundary conditions are imposed on the whole external boundary of the domain. Fluid is injected through an injector I (with rate 0.1 PV per year) and pressure $\phi = 0$ bar is specified at the diagonally opposite producer. Concentration of tracer is determined by solving the transport equation for each time step, using the first order upwind scheme.

1. *Diagonal tensor field:* A diagonal isotropic permeability tensor field is considered for the whole domain. Permeability of the matrix and the fractures is defined as $\boldsymbol{K_m} = \left(\begin{smallmatrix} 1.0 & 0.0 \\ 0.0 & 1.0 \end{smallmatrix} \right)$ mD and $\boldsymbol{K_f} = 10^6 \times \boldsymbol{K_m}$. We solve the problem on the refined (reference) mesh by both the TPS and FPS schemes for reference solutions. The problem is solved on the mixed-dimensional mesh by the hybrid-grid method with TPS and FPS schemes. The pressure solutions obtained by the respective methods are shown in Fig. 15. Tracer concentration contours at PVI= 0.3 resulting from transport corresponding to the respective pressure solutions, are shown in Fig. 16. Plots shown in Fig. 19a show behaviour of the tracer concentration at the producer with respect to time for the respective reference solutions and hybrid-grid methods. For the diagonal isotropic tensor case, both the hybrid-grid TPS and FPS methods yield similar solutions with tracer concentrations in close agreement. Moreover, the behaviour of both solutions is in excellent agreement with the reference solutions.

2. *Full-tensor field:* Now, we consider an anisotropic full-tensor permeability field of relatively weak anisotropy ratio ($10 : 1$ at an angle 30°) for the whole domain. Matrix and fracture permeabilities can be written as $\boldsymbol{K_m} = \left(\begin{smallmatrix} 0.7750 & 0.38971 \\ 0.38971 & 0.3250 \end{smallmatrix} \right)$ mD and $\boldsymbol{K_f} = 10^6 \times \boldsymbol{K_m}$. Fig. 17 shows both the reference pressure solutions and the hybrid-grid pressure solutions. The hybrid-grid TPS method shows some discrepancy in the pressure contours when compared to the hybrid-grid FPS which is in agreement with the reference solution, again showing the benefit of the FPS. Tracer concentration contours at PVI= 0.3 is shown in Fig. 18. Plots of tracer concentration at the producer with respect to time are
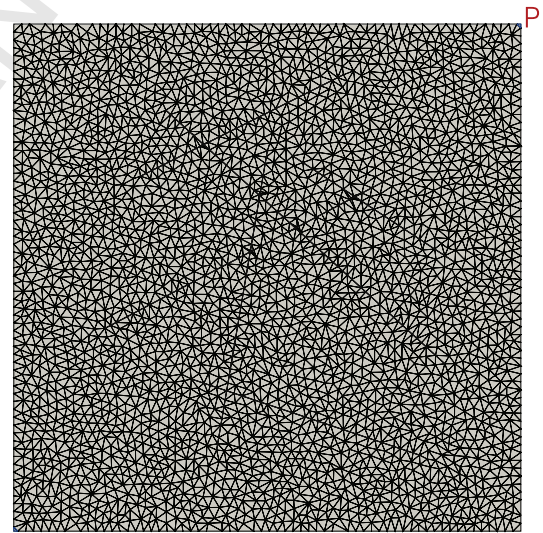
21
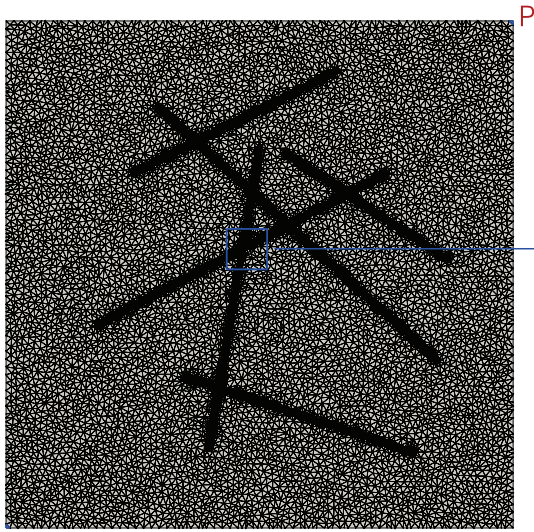
(a) Reference mesh with explicit 2D fracture cells. No. of cells = 61300
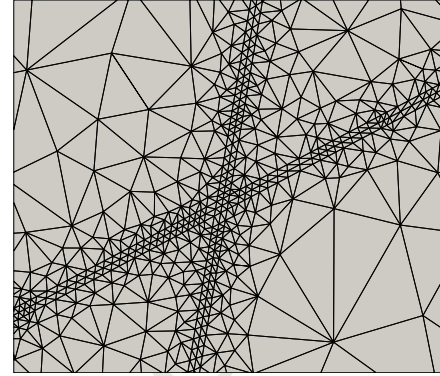
(b) Close up view of a part of the explicit 2D fracture mesh 14a
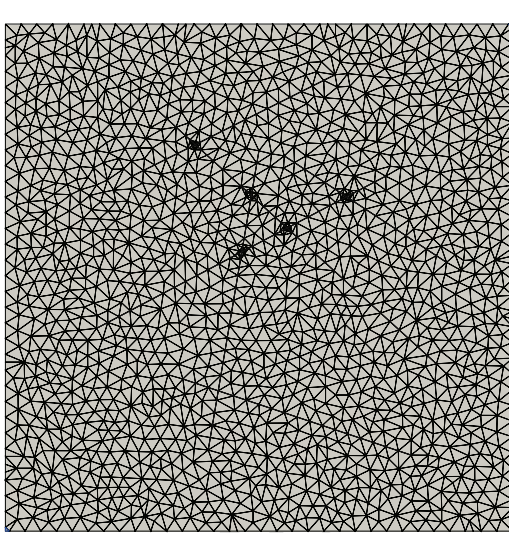
(c) Coarse mixed-dimensional mesh: 3281 2D matrix cells + 185 1D fracture cells

(d) Fine mixed-dimensional mesh: 6332 2D matrix cells + 223 1D fracture cells

Figure 14: Case 2b: A mesh with 2D discretised fractures for reference solutions (a,b) and mixed-dimensional meshes, with 1D fractures, for hybrid-grid method for a domain with multiple intersecting fractures (c,d). Injector is marked by I and producer is marked by P.

given in Fig. 19b. The hybrid-grid FPS method yields a concentration profile at the producer which is in in excellent agreement with the reference solution. The hybrid-grid TPS concentration profile is also close to the FPS profile for this case where $k_f = 10^6$.

3. *Very strong full-tensor field:* Now, we consider a very strong anisotropic full-tensor permeability field (3000 : 1 at an angle 25°) for the whole domain. Matrix permeability is defined by $\boldsymbol{K_m} = \left(\begin{smallmatrix} 0.246436 & .114868 \\ .114868 & 0.053664 \end{smallmatrix} \right)$ mD and fracture permeability is defined by $\boldsymbol{K_f} = k_f \times \boldsymbol{K_m}$ with $k_f = 10^5$. Injection
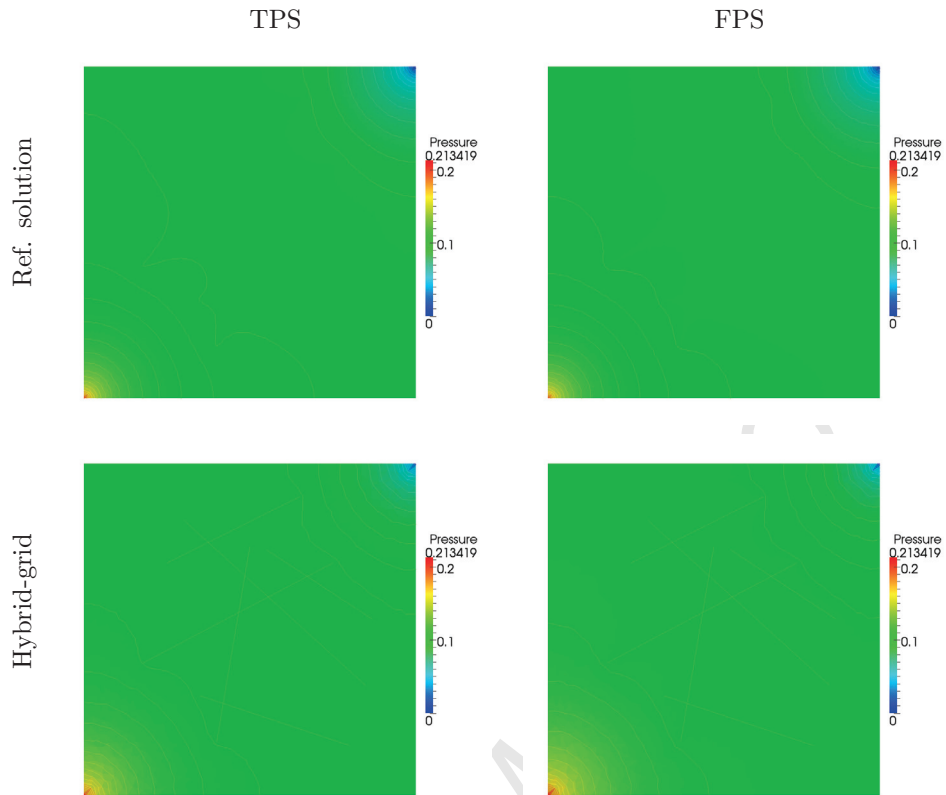
22

Figure 15: Case 2b: Reference pressure solutions computed by the TPS and FPS in first row and pressures computed by the hybrid-grid TPS and FPS in second row for the diagonal isotropic field over a domain with intersecting fractures.

⁴¹⁵ rate is 0.1 PV per year. Fig. 20 shows reference pressure solutions and the hybrid-grid pressure solutions. Both the TPS calculations (Ref. and the hybrid-grid) yield spurious oscillations in the respective pressure solutions whereas hybrid-grid FPS is in agreement with the reference FPS solution, and both of the FPS pressure fields are free of spurious oscillations. Tracer concentrations contours at PVI= 0.1 are shown in Fig. 21. The tracer concentration solution obtained by the hybrid-grid FPS method ⁴²⁰ improves with refinement in the mesh and converges towards the reference solution (Fig. 21) as also indicated by the concentration versus time plots given in Fig. 22. The observed tracer concentration field requires refinement of the matrix mesh for improvement when compared to the reference field.

The results presented, show that the hybrid-grid FPS method produces comparable results to those produced by the hybrid-grid TPS method for cases with diagonal isotropic permeability tensor fields. In cases of ⁴²⁵ anisotropic full-tensor permeability fields, comparison with reference solutions show that the hybrid-grid FPS method yields improved results in contrast to the TPS scheme. The transport solution produced by the hybrid-grid FPS method for intersecting fractures, is in excellent agreement with the behaviour of the reference solution while the TPS scheme shows some discrepancy in the results for full-tensor fields. Moreover, the TPS scheme yields spurious oscillations in the pressure solution for highly anisotropic full-
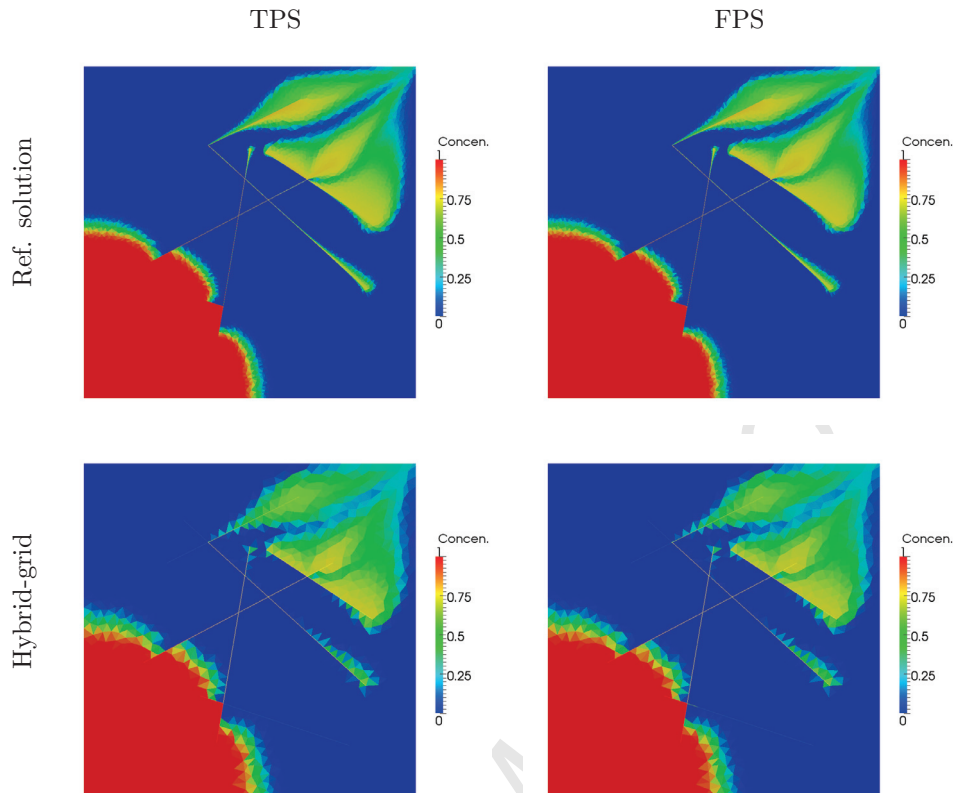
23

Figure 16: Case 2b: Tracer concentration contours at PVI= 0.3 corresponding to the reference pressure solutions in first row and the hybrid-grid TPS and FPS in second row for the diagonal isotropic field over a domain with intersecting fractures.

tensor permeability fields.

5.5. Case 3: Discontinuous strong full-tensor (zigzag) field

Now, we apply the hybrid-grid FPS method to a problem that involves discontinuous and anisotropic full-tensor permeability fields over a fractured domain. The permeability tensor is in a zigzag pattern for the domain that consists of three rock-types as shown in Fig. 23. The anisotropy ratio is 1000 : 1 and the principal axes are oriented at angles of 30°, 120° and 60° for the rock-types from left to right of the concerned domain. There is a horizontal well in the middle of the domain, with fixed pressure $\phi = 300$ bars. The domain consists of various orthogonal intersecting fractures with high permeability of $\boldsymbol{K}_f = 10^4 \times \boldsymbol{K}_m$. The fractures add another local discontinuity to the already discontinuous field. The vertical fractures also intersect with the well. The external boundary of the domain is specified with a low pressure of $\phi = 100$ bar. A boundary-aligned grid is used as shown in Fig. 23. We solve the problem with the FPS scheme ($q_1 = q_2 = 1.0$) for the 2D discretised fractures, to determine a reference solution. We obtain pressure solutions using the TPS ($q = 2/3$) and hybrid-grid FPS ($q_1 = 1.0; q_2 = 0.9$) for comparison. Pressure fields are shown in Fig. 24. The pressure field computed using the hybrid-grid FPS method is in good agreement with the FPS reference solution. There are some oscillations in the TPS pressure field, although the pattern of the pressure field is similar to
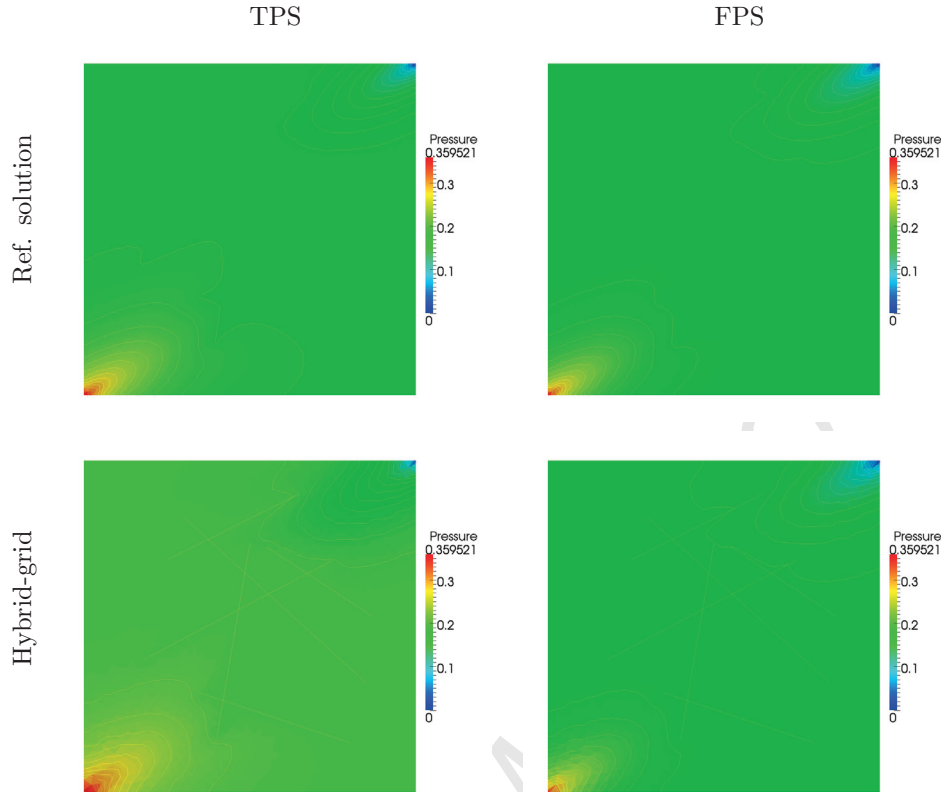
24

Figure 17: Case 2b: Reference pressure solutions computed by TPS and FPS in first row and pressure fields computed by the hybrid-grid TPS and FPS in second row for the anisotropic (10 : 1 at 30°) full-tensor field over a domain with intersecting fractures.

the FPS method. The test case demonstrates the robustness of the hybrid-grid FPS method. This test case provides further evidence of the robustness of FPS [42], now applied to a problem with a discontinuous and strong anisotropic full-tensor permeability field together with fractures and an unstructured grid.

5.6. Case 4: Condition number comparison with 2D gridded fractures

In this section, we compare the condition numbers of the linear system resulting from the hybrid-grid FPS method with the fully gridded equi-dimensional fracture FPS method for a discrete-fracture matrix system. A mesh with gridded 2D fractures and a mesh with 1D fractures is given in Fig. 25. There are two disconnected fracture networks i.e. a large network of four fractures and a second network consisting of two fractures. We solve a channel flow problem with applied horizontal pressure gradient from left to right and no-flow conditions on horizontal outer boundaries. We solve the flow problem for three cases of combinations of conductive fractures and barriers (very low permeable fractures) (i) large network consists of conductive fractures and smaller network consists of barriers (fractures & barriers) (ii) both networks consist of barriers (all barriers) and (iii) both networks consist of conductive fractures (all fractures). Permeabilities of the fractures and the barriers (of aperture $a = 1$ mm) are $\boldsymbol{K}_{f_1} = k_f \boldsymbol{I}$ and $\boldsymbol{K}_{f_2} = (^1/_{k_f})\boldsymbol{I}$. Matrix permeability

25

TPS   FPS
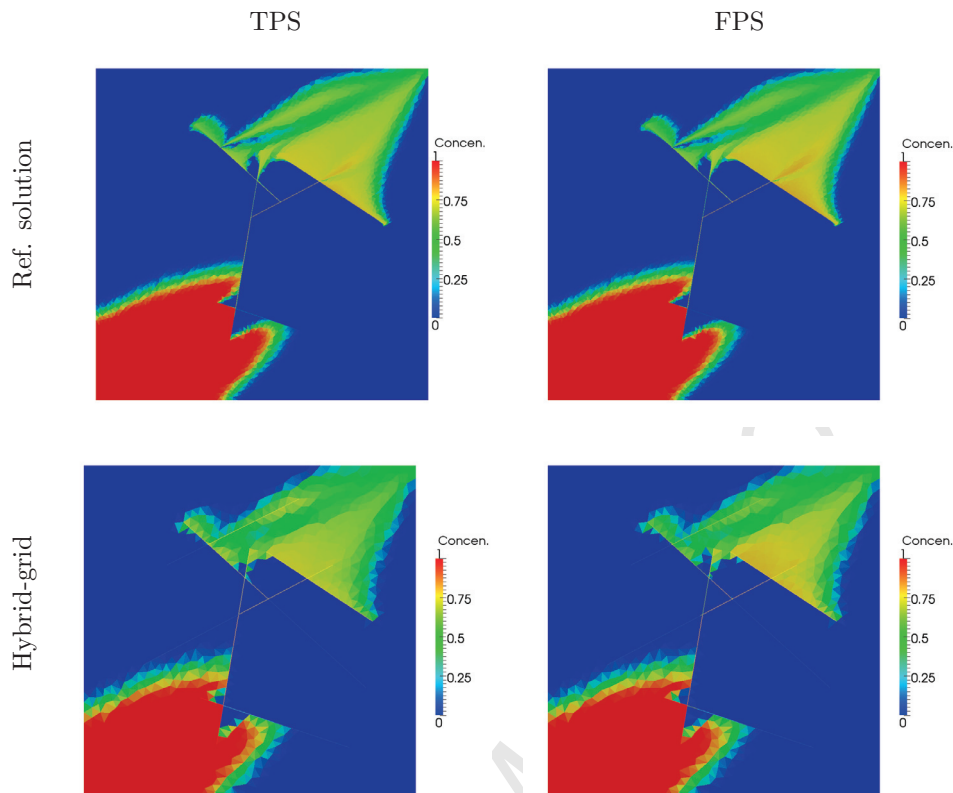
Ref. solution

Hybrid-grid

Figure 18: Case 2b: Tracer concentration contours at PVI= 0.3 corresponding to the reference pressure solutions in first row and the hybrid-grid TPS and FPS in second row for the anisotropic $(10:1$ at $30^o)$ full-tensor field with intersecting fractures.

is $\boldsymbol{K}_m = \boldsymbol{I}$, where I is the identity matrix. The pressure fields computed using the 2D fracture model and the hybrid-grid method for three test cases are presented in Fig. 26. The hybrid-grid FPS method solution is in excellent agreement with the 2D fracture method. The condition numbers for the global linear systems resulting from both methods are given in table 1. Because of the special treatment of cells at junctions of intersecting fractures, the hybrid-grid method yields better conditioned linear systems compared to the 2D fracture method, where fractures are gridded with small cells at the junctions. The condition numbers for the hybrid-grid method are remarkably lower than the 2D fracture method for the cases where barriers are considered.

Fracture model	Frac. & Barr.	Barr. & Barr.	Frac. & Frac.
Hybrid-grid (physical 1D fracture)	2.06e07	1.80e05	4.93e06
2D tris. fracture	4.72e17	2.79e09	2.55e12
2D tris. fracture (square junction cell)	3.34e17	1.49e09	3.39e12
2D quads fracture	2.00e12	2.23e09	1.31e07

Table 1: Case 4: Condition numbers for the hybrid-grid FPS and the equi-dimensional 2D gridded fractures using FPS for a fracture/barrier system with $a = 1$ mm and $k_f = 10^6$. (Condition number of a sparse matrix G is computed by the Matlab command *condest(G,4)*).
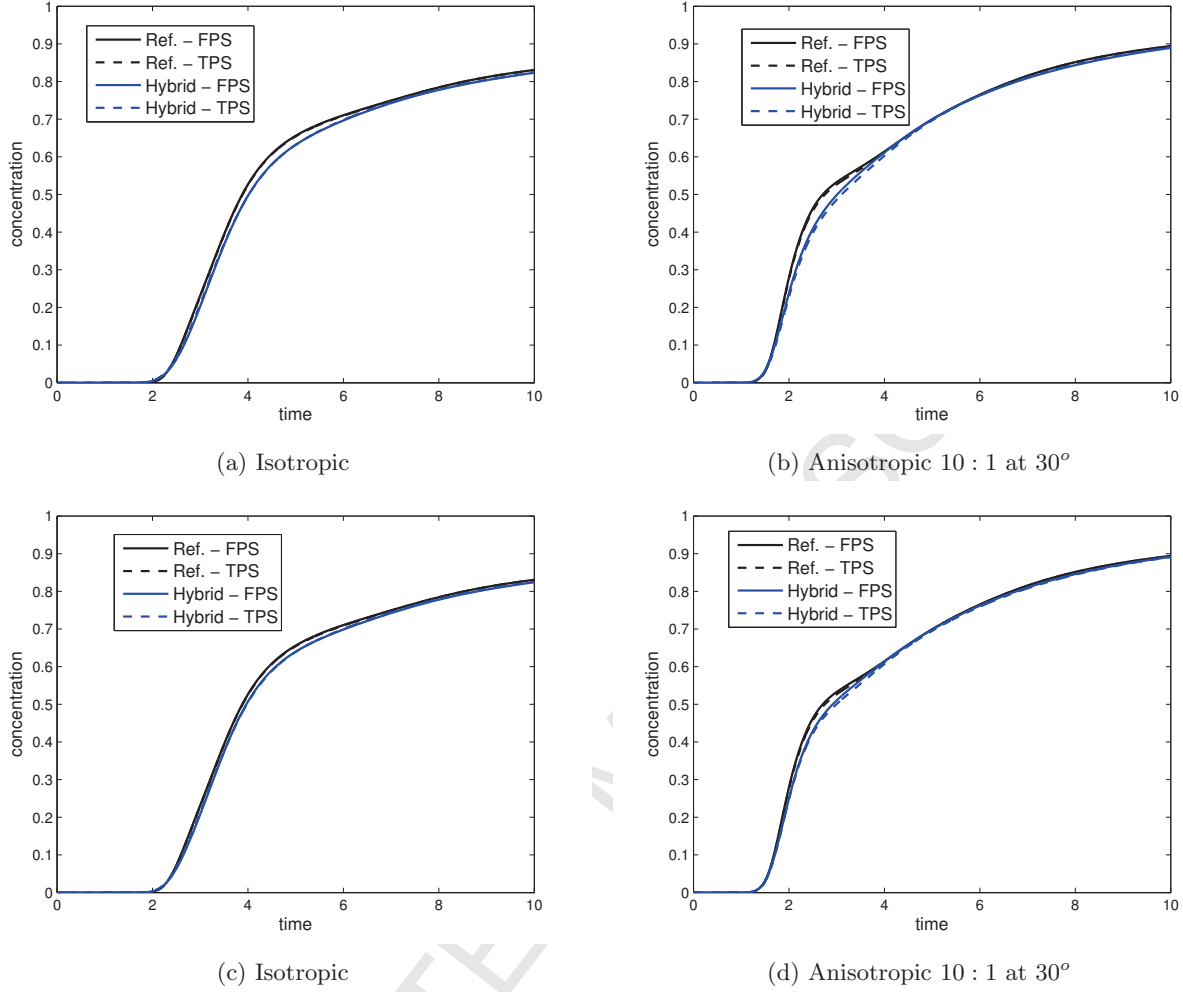
26

Figure 19: Case 2b: Tracer concentration at producer versus time (years) corresponding to the reference pressure solutions of the TPS and FPS and the hybrid-grid TPS and FPS pressure solutions for a domain with intersecting fractures. Results of hybrid-grid method in (a) & (b) are for coarse mesh (Fig. 14c) and results of hybrid-grid method in (c) and (d) are for fine mesh (Fig. 14d).

5.7. Case 5: Compressible gas flow

In this case, we consider a isothermal compressible gas flow simulation. The general equation is written in terms of the pressure as:

$$c_t \frac{\partial \phi}{\partial t} - \nabla \cdot (\boldsymbol{\lambda} \nabla \phi) = \frac{RT}{M} q_c \tag{16}$$

470 where M is the molecular weight of the gas, R is the ideal gas constant, T is the temperature of the gas and is assumed constant here. Z is the gas compressibility factor, $c_t = \frac{\varphi}{Z} \left(1 - \frac{\phi}{Z} \frac{dZ}{d\phi} \right)$, $\boldsymbol{\lambda} = \frac{\phi}{\mu Z} \boldsymbol{k}$ and φ is porosity. As c_t and diffusivity $\boldsymbol{\lambda}$ both depend on the pressure of the gas so that Eq. (16) is a non-linear parabolic partial differential equation which has more complexity and computational cost for solution compared to the previous linear pressure equation. We use the Peng-Robinson [49] equation of state for

475 the relationship between compressibility factor Z and the pressure ϕ that has also been used in [50]. The relationship is a cubic equation that can be solved for Z for the given ϕ of real-gas by Cardano's method or
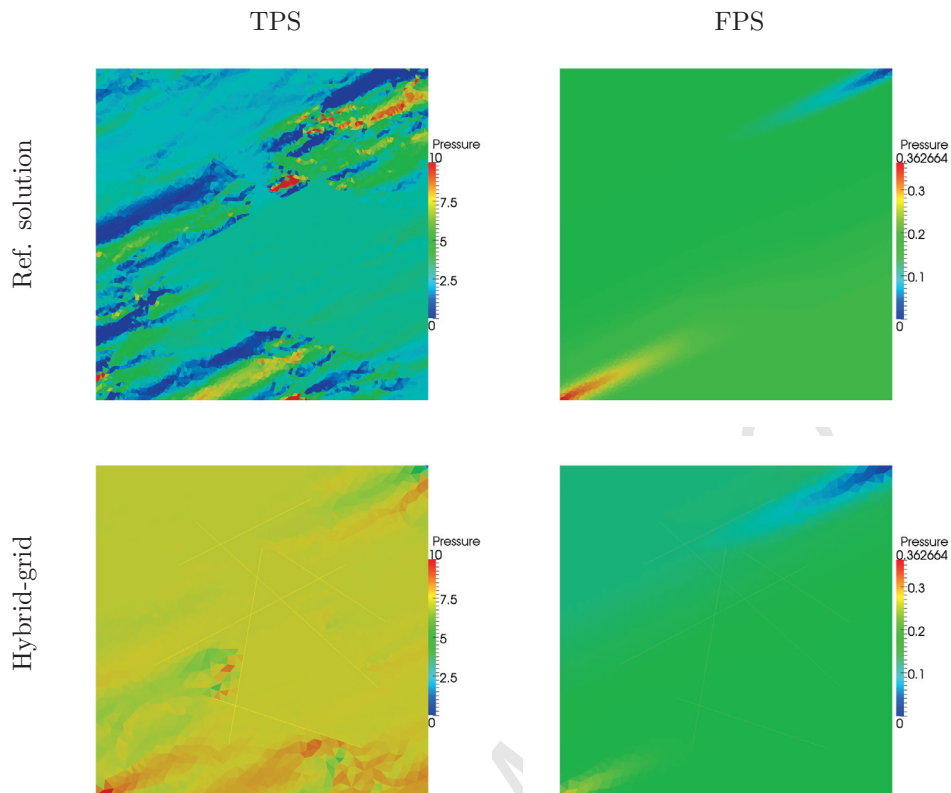
TPS   FPS

Figure 20: Case 2b: Reference pressure solutions using TPS and FPS in first row and pressures computed by the hybrid-grid TPS and FPS in second row for the anisotropic (3000 : 1 at 25°) full-tensor field over a domain with intersecting fractures.

by the Newton-Raphson method numerically [51, p. 19].

To compute the discrete solution of the non-linear transient pressure problem, governed by Eq. (16), we use the above hybrid-grid FPS spatial discretisation (section 4.3) that is developed to approximate Eq. 1 in fractured media, now with the diffusivity coefficient ($\frac{\boldsymbol{k}}{\mu}$) replaced by $\boldsymbol{\lambda}$ together with source term $\frac{RT}{M}q_c$ on the right hand side. We use a semi-implicit discretisation in time (with spatial hybrid-grid FPS discretisation for fractured media) expressed as:

$$\frac{1}{\delta t}M^{n+1}(\Phi^{n+1} - \Phi^n) + G^n\Phi^{n+1} = \bar{\boldsymbol{q}}_c \qquad \text{for time step } n \tag{17}$$

where, M^{n+1} is a diagonal system of integrated coefficients $c_t(\phi^{n+1})$ over all matrix and fracture cells. Eq. (17) is solved for all the unknown matrix and fracture pressures (Φ^{n+1}) at the new time-step. The first part of Eq. (17) is a function of unknown Φ^{n+1} where $c_t = \frac{\varphi}{Z}\left(1 - \frac{\phi}{Z}\frac{dZ}{d\phi}\right)$ while the second part is a function of the known Φ^n where $\boldsymbol{\lambda} = \frac{\phi}{\mu Z}\boldsymbol{k}$. To solve the non-linear equation in terms of Φ^{n+1}, we employ the Newton-Raphson method at each time step. We use the PETSc [52] library for the solution of the linear systems involved in the Newton-iteration. As the linear systems are in general non-symmetric, we solve the systems via GMRES [53] preconditioned by incomplete LU factorization (iLU) or the algebraic multigrid

28

Ref. solution using mesh with 2D fractures shown in Fig. 14a
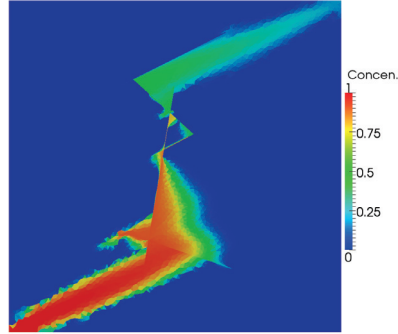
Hybrid-grid method using coarse mesh shown in Fig. 14c

TPS   FPS
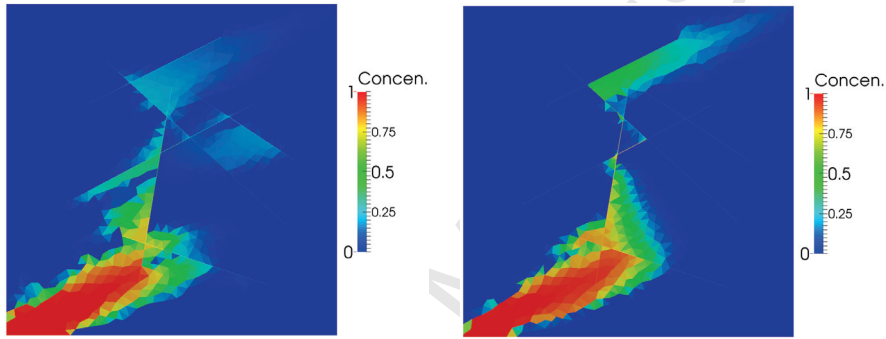
Hybrid-grid method using fine mesh shown in Fig. 14d

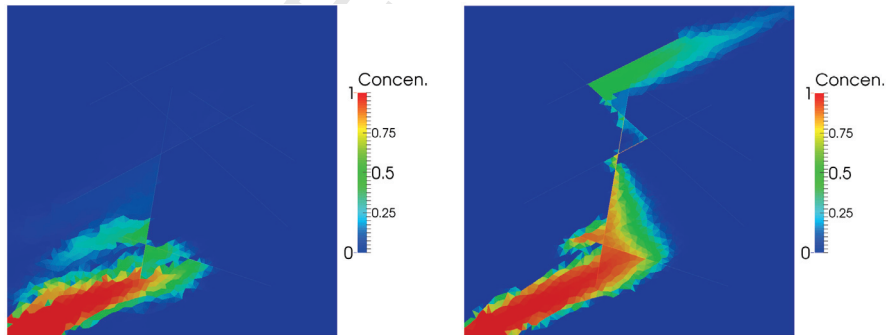TPS   FPS

Figure 21: Case 2b: Tracer concentration contours at PVI= 0.1 for the reference pressure solutions in first row and for the hybrid-grid TPS and FPS in second row for the anisotropic (3000 : 1 at 25°) full-tensor field over a domain with intersecting fractures.

490 ($gamg$) provided in the PETSc library. Initial conditions and boundary conditions are given below.

We consider a synthetic domain containing a fractured reservoir as shown in the Fig. 27 which represents the 2D plane with a well along the left side wall. There are highly conductive interconnected and intersecting fracture networks throughout the domain. The reservoir is full of *methane gas, CH_4* at the initial reservoir pressure of $\phi(x, y, 0) = 20$ bar and constant temperature of 330 K. The well at the left boundary of the
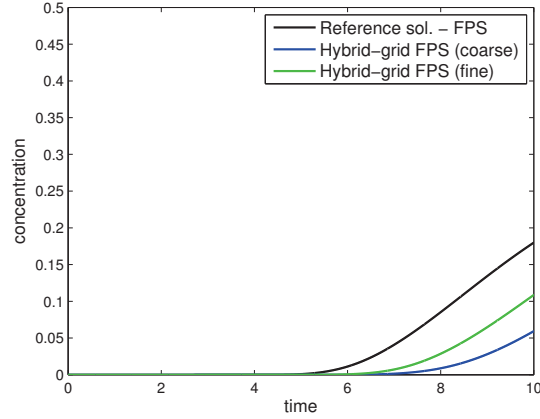
Figure 22: Case 2b: Tracer concentration at producer versus time (years) for the reference pressure solutions and the hybrid-grid pressure solutions over the coarse mesh shown in Fig. 14c (blue plot) and the fine mesh shown in Fig. 14d (green plot) for the case of very strong anisotropic (3000 : 1 at 25°) full-tensor permeability field.
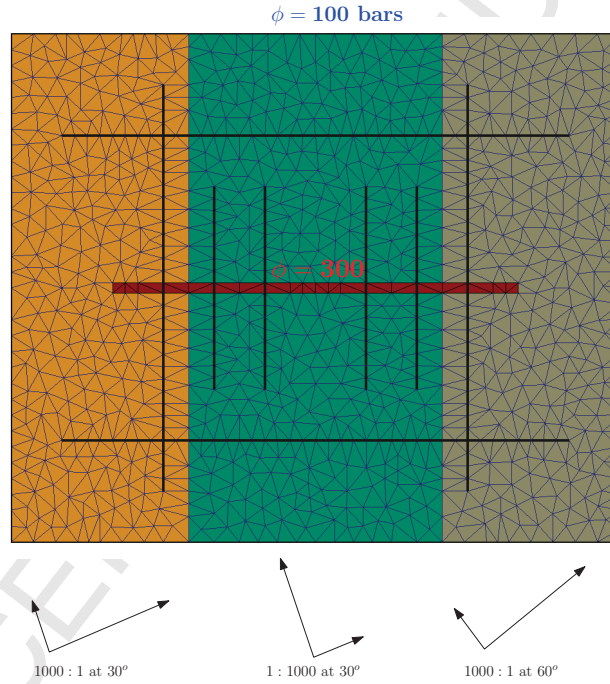

Figure 23: Case 3: Fractured domain with discontinuous full-tensor (zigzag) permeability field. There is a horizontal well in the middle intersecting with the fracture networks.

domain is at the low pressure of $\phi(0, y, t) = 3.39$ bar and acts as the producing well for the reservoir. The other three boundaries are assigned no-flow boundary conditions. The properties of the methane gas [54] are as follows:

Critical pressure and temperature: $\phi_{cr} = 45.99$ bar, $T_{cr} = 190.55$ K

Ascentric-factor $\omega = 0.008$; viscosity $\mu = 0.011$ cP

The matrix has a strong anisotropic and heterogeneous permeability defined via $\boldsymbol{k_m} = \begin{pmatrix} 1+2\tilde{x}^2+\tilde{y}^2 & 4\tilde{x}\tilde{y} \\ 4\tilde{x}\tilde{y} & 1+\tilde{x}^2+2\tilde{y}^2 \end{pmatrix}$ mD

where, $\tilde{x} = x/670.56$, $\tilde{y} = y/365.76$. The non-linear relationship between the compressibility factor and the

30
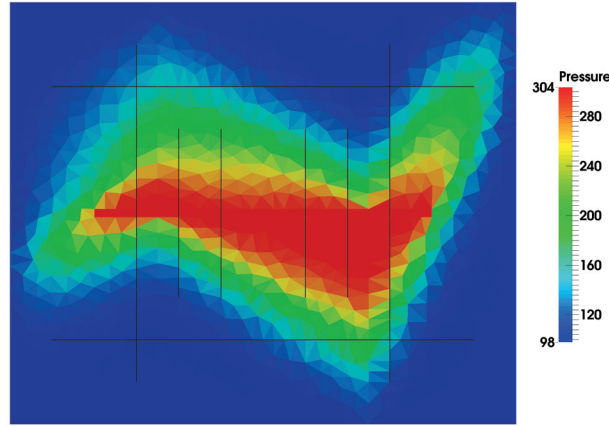
(a) Ref. pressure solution by the FPS with 2D discretised fractures. $q_1 = q_2 = 1.0$
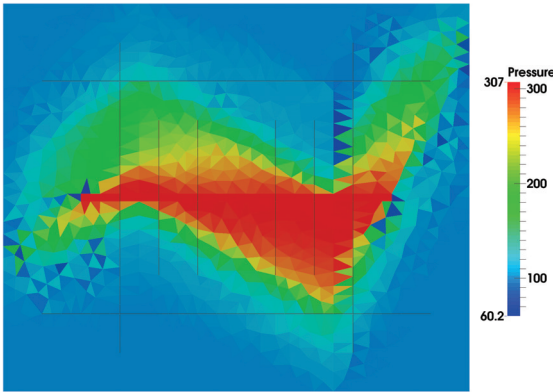
(b) Pressure solution by the hybrid-grid TPS with 1D physical fractures. $q_1 = 2/3$
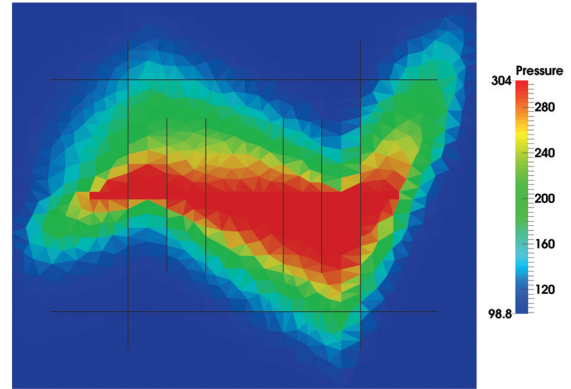
(c) Pressure solution by the hybrid-grid FPS with 1D physical fractures. $q_1 = 1.0; q_2 = 0.9$

Figure 24: Case 3: Pressure solutions for the discontinuous full-tensor (zigzag) permeability field

pressure is given by the Peng-Robinson equation of state.

The fracture has the higher permeability with $k_f = 10^6 \times k_m$. And, all the fractures are assigned an aperture of $a = 1$ mm. The whole domain is discretised using a triangular mesh with fractures as lower-dimensional internal boundary constraints. The boundary-aligned mesh of the fractured domain is shown in Fig. 28. The transient pressure problem is solved for 2 years of production by hybrid-grid FPS method, for the cases of (i) the reservoir with fractures and (ii) the same reservoir without fractures.

The pressure contour plots at the intermediate times are shown in Fig. 29. Flow of methane propagates rapidly through the highly conductive fractures, noticeably, in those fractures which are directly connected to the low-pressure boundary (well). The behaviour of the pressure propagation is highly influenced by the heterogeneity of the matrix and the high permeability of fractures. The pressure plots show the influence

31
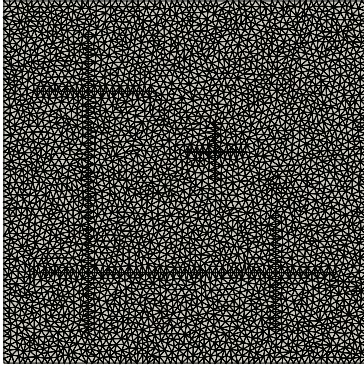
(a) Mesh with 2D gridded fractures. 8400 2D triangular cells
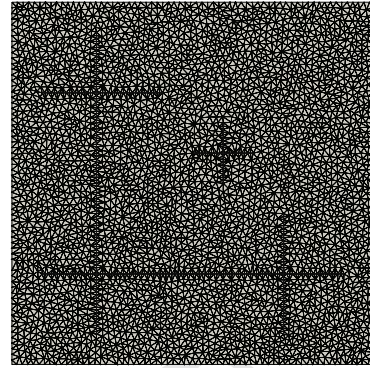
(b) Mesh with 1D fractures. 7766 2D triangular cells + 320 1D cells

Figure 25: Case 4: (a) A mesh with 2D gridded fractures and (b) a mixed-dimensional mesh with 1D fractures. Fracture cell length along the fracture in both meshes is equal.

of the presence of the fractures. Moreover, there is higher production from the fractured reservoir because of the fractures compared to the reservoir without fractures. Fig. 30 shows the semi-log plots of average reservoir pressure and the production rate with respect to time for the cases of the reservoirs with fractures and without fractures. The average pressure of the fractured reservoir decreases rapidly with time and approaches the pressure of the producer, when compared to the reservoir without fractures, which takes a longer period of time to approach to the low pressure of the producer. Moreover, we have higher production rate with fractures compared to no fractures, where production rate declines sharply during early time then approaches an equilibrium state. In our experience production of fractured reservoirs are highly dependent on fracture network connectivity together with connectivity to producers. Note that, the computational cost of the compressible methane gas flow solution in the fractured reservoir is ~ 2.56 times the computational cost for computing flow in the reservoir without fractures. Finally, we note that in contrast to the FPS simulation, the earlier TPS method yields spurious oscillations for this case, resulting in negative pressures causing the simulation to fail, illustrating a further benefit of the new hybrid-grid FPS formulation.

6. FPS coupled with a lower-dimensional fracture model

In the previous section, we have presented and analysed the hybrid-grid method for CVD-MPFA with full pressure support (we denote by FPS). In the above method, the 2D pressure equation is solved in both rock-matrix and fracture by the usual FPS formulation. In this section, we investigate and analyse an FPS formulation coupled to a lower-dimensional fracture model, analogous to the formulation in the context of the TPS presented in [33, 34] and the mixed finite-element presented in [10]. For the matrix domain an nD equation is solved while an (n-1)D equation is solved for fracture cells. The single phase conservation laws
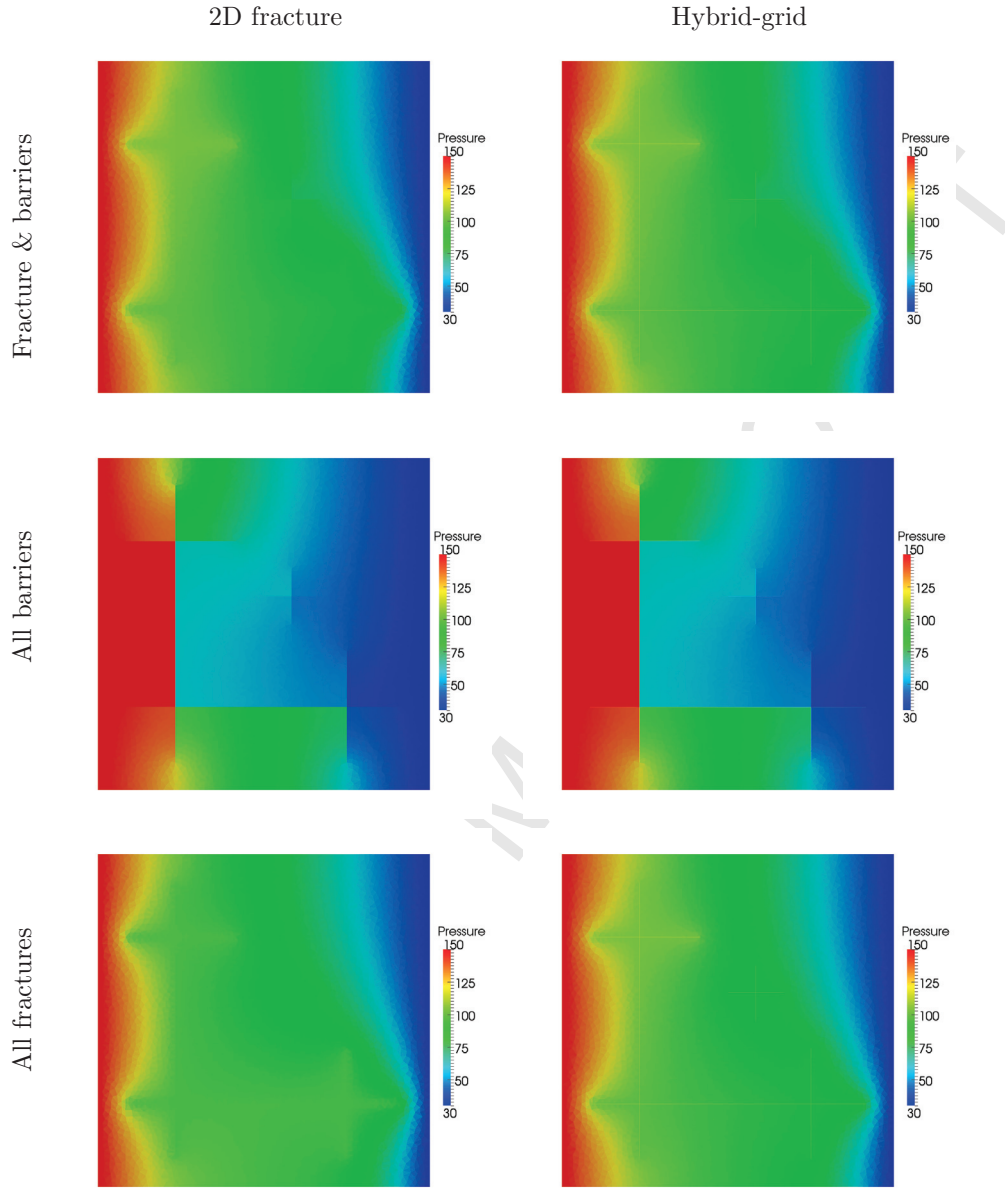
32

Figure 26: Case 4: Pressure solutions computed by the 2D fracture method and the hybrid-grid method for aperture $a = 1$ mm and $k_f = 10^6$ for three different cases of fractures and barriers.

are written as:

$$-\nabla \cdot \boldsymbol{K}_m \nabla \phi \quad = \quad q_{cm} \quad \text{in} \quad \Omega_m \tag{18}$$

$$-\nabla_t \cdot \boldsymbol{K}_{f,t} \nabla_t \phi_f + q_f \quad = \quad q_{cf} \quad \text{in} \quad \Omega_f \tag{19}$$

where ∇_t and $\boldsymbol{K}_{f,t}$ are the respective longitudinal (tangential) gradient operator and permeability of the fractures. q_{cm} and q_{cf} are known source terms for the rock matrix and the fracture respectively. Transfer
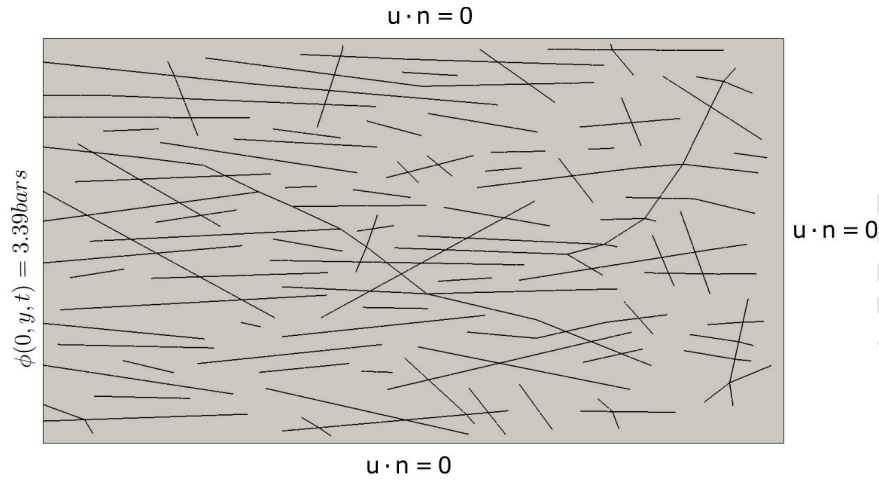
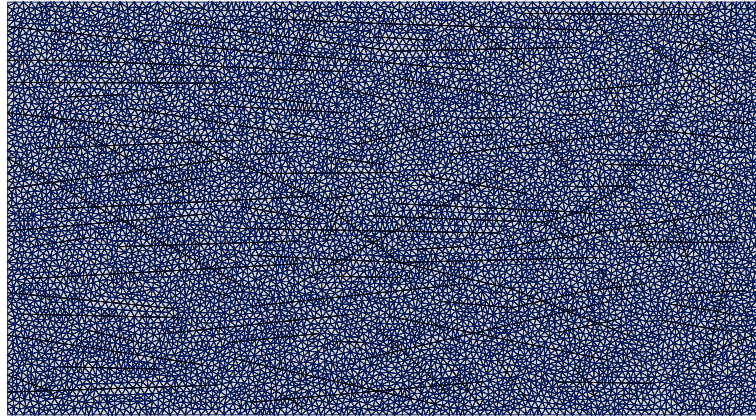Figure 27: Case 5: Methane gas reservoir: $[0, 670.56] \times [0, 365.76]$ m^2

Figure 28: Case 5: Boundary-aligned mesh of the fractured Methane reservoir.(19549 triangles + 2495 fracture edges)

function, q_f, accounts for the net normal flux transfer between matrix and fracture cells, resulting from the dimensionality reduction to obtain (n-1)D equation (19). The matrix-fracture flux is also added naturally in the formulation for the matrix cells. The flow equations (18) and (19) are integrated over the grid cell control volumes using the Gauss divergence theorem to obtain,

$$-\oint_{\delta\Omega_{m_i}} (\boldsymbol{K}_m \nabla\phi) \cdot \boldsymbol{n}_i dS = \bar{q}_{cm} \tag{20}$$

$$-\oint_{\delta\Omega_{f_j}} (\boldsymbol{K}_{f,t} \nabla_t \phi_f) \cdot \boldsymbol{n}_j dS + Q_f = \bar{q}_{cf} \tag{21}$$

where $\bar{q}_{cm} = \int_{\Omega_{m_i}} q_{cm}\, dV$ and $\bar{q}_{cf} = \int_{\Omega_{f_j}} q_{cf}\, dV$ are respective specified source terms for the matrix and fracture cells Ω_{m_i}, Ω_{f_j}. Moreover, $Q_f = \int_{\Omega_{f_j}} q_f\, dV$, is the transfer function resulting from the net flux normal to the lower-dimensional fracture cell Ω_{f_j}. Note that as a consequence of the lower-dimensional
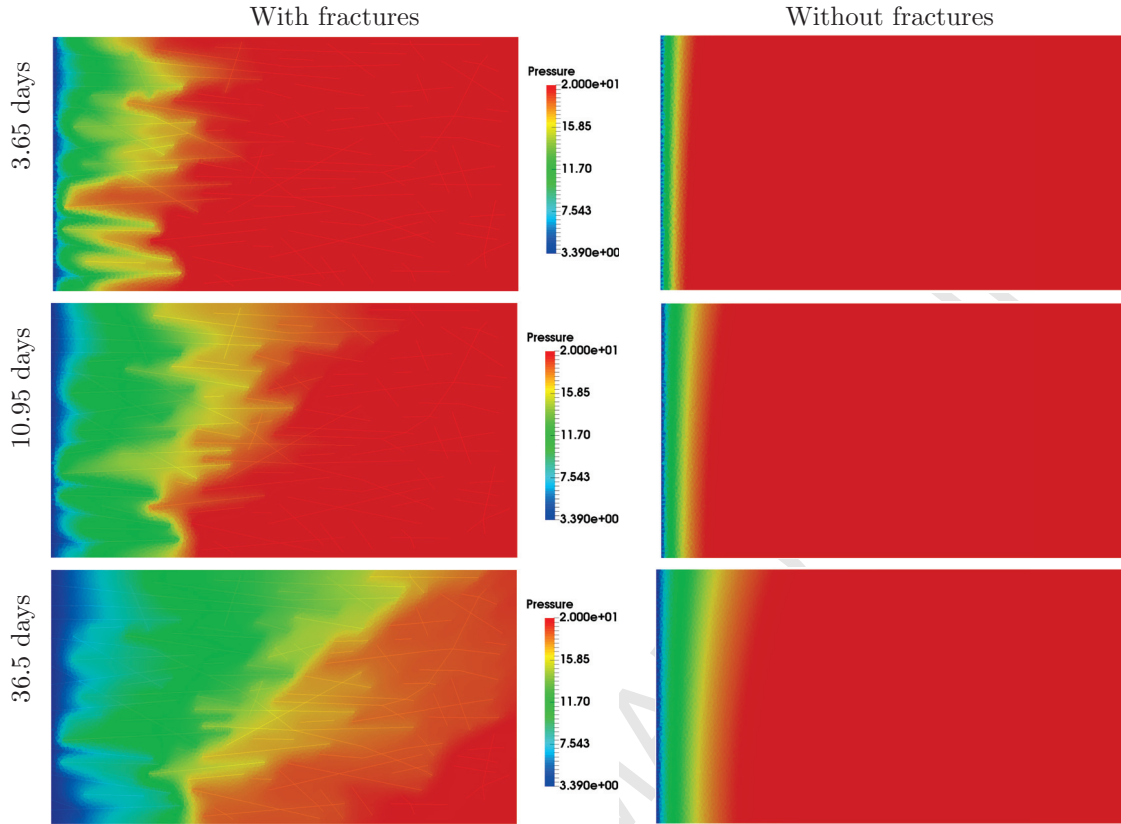
34

Figure 29: Case 5: Transient pressure solutions of the compressible methane gas production from the fractured and non-fractured reservoirs
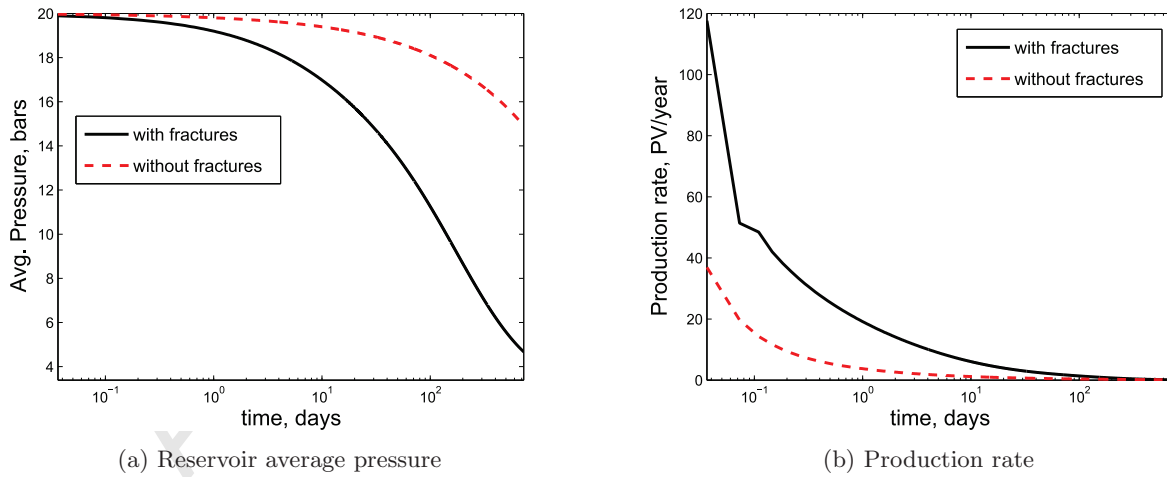

(a) Reservoir average pressure

(b) Production rate

Figure 30: Case 5: Plots of average pressure ($\bar{\phi} = \frac{\sum_{i=1}^{N} V_i \phi_i}{\sum_{i=1}^{N} V_i}$, where N is the total number of cells (matrix and fracture) in the mesh, V_i is the volume of a cell i and ϕ_i is the pressure of a cell i) and production rate of the fractured and non-fractured methane reservoirs with respect to time

fracture model, the model will only be consistent if the permeability tensor is diagonal in the frame of the fracture (which corresponds to the geologically natural case). The effect of the lower-dimensional assumption

35

is considered in a number of examples below.

6.1. Flux approximation

We present the FPS formulation for the reduced dimensional fractures in a cluster shown in Fig. 31a. The dual-cell for the cluster is also shown in Fig. 31a by the dashed-line polygon. The sub-cells are not modified in any way. Pressure unknowns are associated with the centroids of the nD matrix cells. Pressure points are also defined for the sub-interfaces, on midpoints of the edges. An additional unknown pressure is also defined at the cluster vertex that is common to all the cells in the cluster. Full pressure continuity is imposed on all the sub-interfaces between the matrix sub-cells. For each of the matrix sub-cells, full pressure support is defined by the pressure points at the cell centre, the right-edge, the left-edge and the auxiliary pressure at the vertex. The full pressure support of cells 1 and 2 is depicted in Fig. 31b. Discrete piecewise fluxes on
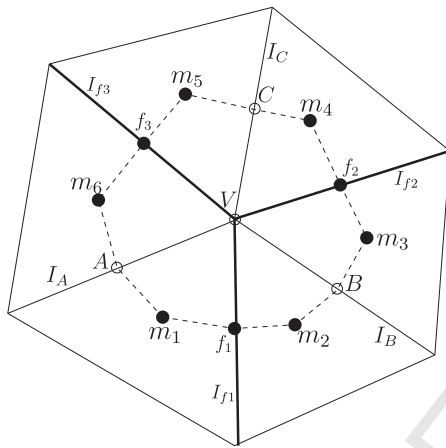
(a) Cluster of matrix cells involving fracture cells as interfaces in between, depicted by bold lines. Fluxes are discontinuous across fracture-interfaces, but pressure is continuous.
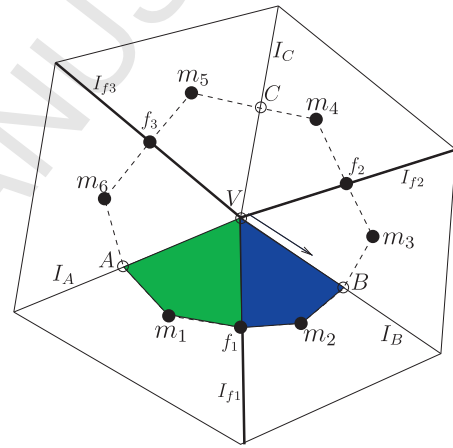
(b) Dual cell with sub-cells of matrix cells. Full pressure supports (FPS) are also shown for matrix cells 1 and 2.
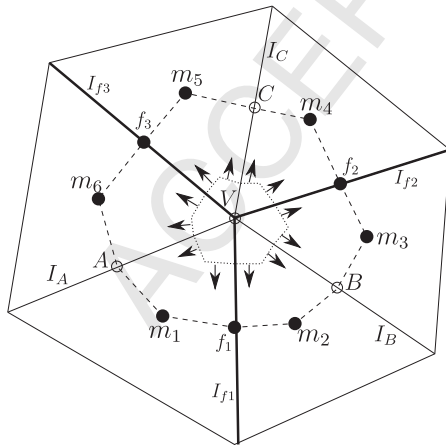
(c) Auxiliary control-volume around the cluster vertex is shown.
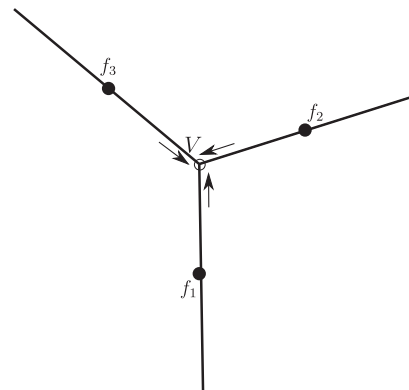
(d) Cluster of fracture cells only.

Figure 31: Cluster and dual-cell involving fracture cells as interfaces. A cluster of fractures is also shown.

the sub-interfaces are determined in the same way as shown in sub-section 3.2. Flux on a sub-interface from
full pressure support in a sub-cell, is dependent on the (primal) cell-centre pressure, sub-interface auxiliary
pressures and the vertex auxiliary pressure. If any of the sub-interfaces lies on a 1D fracture, then the (primal)
pressure of that fracture cell will be involved in the flux approximation. We assume that the fractures are
highly conductive so pressure is constant across the width of the fracture. Fluxes are discontinuous on the
sub-interfaces aligned with fractures. For the concerned cluster of cells, we require 3 (continuous) fluxes on
the left side of sub-interfaces which are not fractures and 6 fluxes corresponding to both the sides (right
and left) of the sub-interfaces aligned with the fractures and are formulated in a combined simple form of
matrices, as:

$$\boldsymbol{F} = A^{9\times6}\Phi_m + B^{9\times4}\Phi_I + C^{9\times3}\Phi_f \tag{22}$$

where, $\Phi_m = (\phi_{m_1}, \phi_{m_2}, \phi_{m_3}, \phi_{m_4}, \phi_{m_5}, \phi_{m_6})^{tr}$ are pressures associated with the matrix cells, $\Phi_I = (\phi_A, \phi_B,$
$\phi_C, \phi_V)^{tr}$ are auxiliary pressures on the sub-interfaces which are not fracture cells and the cluster vertex
V, and $\Phi_f = (\phi_{f_1}, \phi_{f_2}, \phi_{f_3})^{tr}$ are pressures associated with the involved fracture cells. As in the usual
CVD-MPFA formulation, continuity of flux is imposed on each of the sub-interfaces that are not fractures.
In FPS, the divergence free condition of the partial differential equation over an auxiliary dual-cell is also
utilized (Fig. 31c) written as $-\oint_{\partial\tilde{\Omega}_{i_{AUX}}} (\boldsymbol{T}\tilde{\nabla}\phi)\cdot\boldsymbol{n}dS = 0$ for a small auxiliary control-volume $\tilde{\Omega}_{i_{AUX}}$ defining
the auxiliary dual-cell surrounding the vertex of the cluster. In this way, Φ_I are eliminated by imposing
continuity of fluxes defined on both sides of the rock matrix sub-interfaces, and the divergence free condition
over the auxiliary control-volume. As a result, the fluxes are now expressed in terms of primal unknowns
Φ_m and Φ_f only, as follows:

$$\boldsymbol{F} = \bar{A}^{9\times6}\Phi_m + \bar{C}^{9\times3}\Phi_f \tag{23}$$

Fluxes on the sub-interfaces of fractures, are retained as discontinuous. The sum of the negative of these
discontinuous fluxes on both sides of the fracture-interfaces form one half of the transfer functions for the
corresponding 1D fracture cells. At interface I_{f_1}, the sum of the negative of the discontinuous fluxes is
defined as half of the transfer function for the fracture cell f_1:

$$Q_{f_1,1/2} = -F_{I_{f1}}^1 - F_{I_{f1}}^2 \tag{24}$$

In the same way we can determine the half transfer functions for other fracture cells (as interfaces) involved
in the cluster. As the fluxes have already been determined in terms of Φ_m and Φ_f in an analogous form to
Eq. (23), so we can write the system of half transfer functions for the corresponding fracture cells in terms
of Φ_m and Φ_f as follows;

$$\boldsymbol{Q}_{f,1/2} = -\boldsymbol{F}_L - \boldsymbol{F}_R \tag{25}$$

37

which in the above case leads to

$$\boldsymbol{Q}_{f,1/2} = \bar{D}^{3\times6}\Phi_m + \bar{E}^{3\times3}\Phi_f \tag{26}$$

Fracture-fracture fluxes

A cluster of three 1D fracture cells is represented in Fig. 31d. Pressure is approximated at the midpoint of the fractures. A discrete pressure is also added at the interface face (vertex in 1D) where fractures intersect each other. The outgoing fluxes are determined for every 1D fracture at the vertex, e.g for fracture f_1 we have,

$$\mathcal{F}_V^1 = -K_{f,t}(\phi_V - \phi_{f_1})\frac{a}{L_f} \tag{27}$$

where ϕ_{f_1} is the pressure associated with the mid-point of the fracture cell, ϕ_V denotes the pressure at the common vertex of the fracture cells. a denotes the given aperture of the fracture and L_f is half of the length of the fracture cell f_1. Outgoing fluxes of the fracture cells f_2 and f_3 are defined in similar fashion. All the fluxes can be formulated in combined form as follows:

$$\boldsymbol{\mathcal{F}} = A^{3\times3}\Phi_f + B^{3\times1}\phi_V \tag{28}$$

where, $\Phi_f = (\phi_{f_1}, \phi_{f_2}, \phi_{f_3})^{tr}$. The pressure at the intermediate vertex is eliminated by imposing the condition of mass conservation at the vertex analogous to Kirchhoff's current law with

$$\sum_{k=1}^{3} \mathcal{F}_k = 0 \tag{29}$$

leading to

$$\phi_V = \left(B_V^{1\times1}\right)^{-1} A_V^{1\times3}\Phi_f$$

Fluxes are then expressed in terms of fracture cell pressures and consequently

$$\boldsymbol{\mathcal{F}} = \bar{A}^{3\times3}\Phi_f \tag{30}$$

Note that, the above fracture-fracture flux formulation can be easily generalized to a cluster with any number of fracture cells. For a cluster of only two fracture cells, condition (29) is equivalent to the continuity of fluxes between two fracture cells.

Having determined the matrix fluxes, the fracture transfer functions and the fracture fluxes, we can complete the discrete scheme to form the discrete divergence equation for every matrix cell and fracture cell. As a

38

result, we obtain a coupled linear system of the form:

$$\begin{pmatrix} G_{mm} & \mathcal{G}_{mf} \\ \mathcal{G}_{Tm} & \bar{G}_{ff} \end{pmatrix} \begin{pmatrix} \Phi_m \\ \Phi_f \end{pmatrix} = \begin{pmatrix} \bar{\boldsymbol{q}}_{cm} \\ \bar{\boldsymbol{q}}_{cf} \end{pmatrix} \tag{31}$$

The above coupled system, (31) can be solved by iterative solution methods for matrix and fracture pressures. It is noted that a smaller linear system is solved locally, for every cluster compared to the hybrid-grid method because of the lower-dimensional fracture cells. Matrix-matrix fluxes and matrix-fracture fluxes in (23) and fracture-fracture fluxes in (30) can be determined separately in parallel and assembled into the coupled linear system (31).

6.2. Case 6: Comparison between hybrid-grid FPS and FPS coupled with 1D fracture model

The pressure equation and the respective tracer transport equation are solved via FPS coupled with the lower-dimensional (1D) fracture model. We compare FPS coupled with the lower-dimensional (1D) model versus the hybrid-grid FPS method. We solve injector-producer problems for various cases of diagonal isotropic and anisotropic full-tensor permeability fields. We solve problems, with multiple 1D fractures, over the meshed domain shown in Fig. 14c, that has been used in section 5.4 (Case 2b: Multiple intersecting fractures). Zero-flux boundary conditions are imposed on all external boundaries of the domain. Fluid is injected through an injector I (with rate 0.1 PV per year) and pressure $\phi = 0$ bar is specified at the producer. Concentration of tracer is determined by solving the transport equation for each time step, using the first order upwind scheme.

6.2.1. Case 6a: Diagonal tensor field

A diagonal isotropic permeability tensor field is considered for the whole domain. Permeability of the matrix and the fractures is defined by $\boldsymbol{K_m} = \left(\begin{smallmatrix} 1.0 & 0.0 \\ 0.0 & 1.0 \end{smallmatrix} \right)$ mD and $\boldsymbol{K_f} = 10^6 \times \boldsymbol{K_m}$, respectively. Fig. 32 shows the pressure solutions obtained via the hybrid-grid FPS method and the lower-dimensional (FPS) fracture model. Respective tracer concentration contours at PVI= 0.3 are also given. Plots of tracer concentration at the producer with respect to time are shown in Fig. 38a. The lower-dimensional fracture model (1D fracture) yields results that are in excellent agreement with the hybrid-grid FPS method. The lower-dimensional fracture model has less degrees of freedom and computational cost locally for a dual-cell compared to the hybrid-grid method.

6.2.2. Case 6b: Full-tensor field ($10:1$ at 30°)

The next case involves a full-tensor permeability field with relatively weak anisotropy ratio $10:1$ at 30° to the horizontal over the whole domain. The matrix and the fractures are assigned the permeability tensor of $\boldsymbol{K_m} = \left(\begin{smallmatrix} 0.7750 & 0.38971 \\ 0.38971 & 0.3250 \end{smallmatrix} \right)$ mD and $\boldsymbol{K_f} = 10^6 \times \boldsymbol{K_m}$, respectively. The results of the 1D fracture model conform to the results produced by the hybrid-grid FPS method for this mild full-tensor case, as shown in Fig. 33 and Fig. 38b.
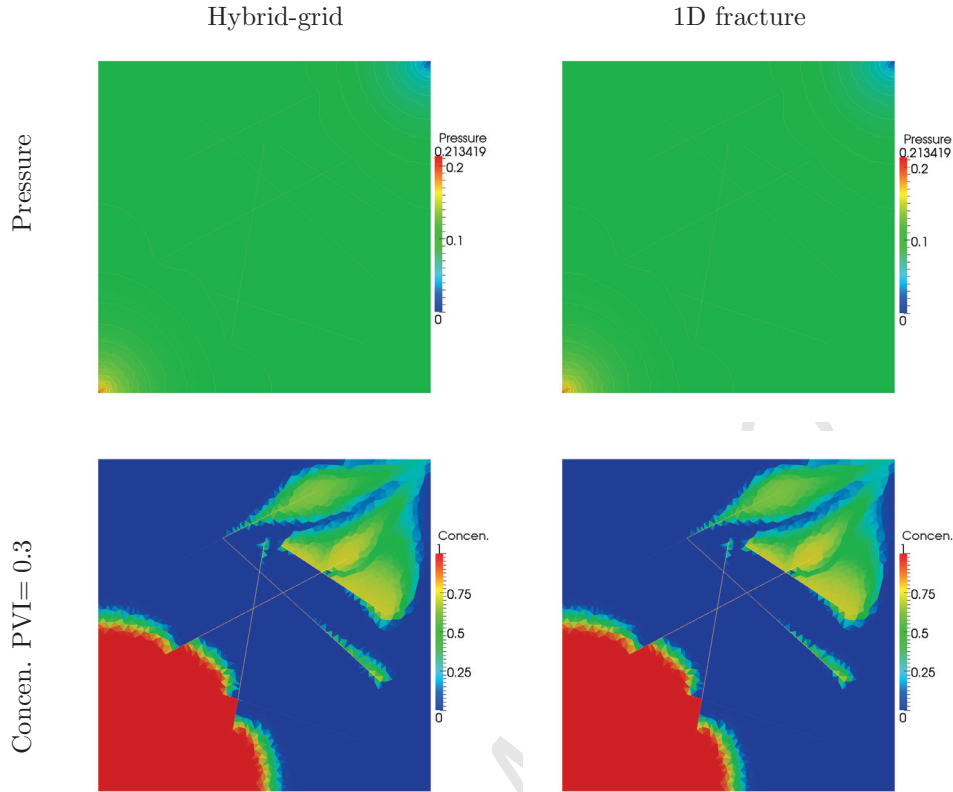
39

Figure 32: Case 6a: Pressure solution and tracer concentration contours (PVI= 0.3) obtained by the hybrid-grid FPS and the (FPS) 1D fracture model for a diagonal isotropic field with multiple intersecting fractures.

6.2.3. Case 6c: Strong full-tensor field ($1000 : 1$ at 30°)

In this case, we solve a problem with a strong full-tensor permeability field with anisotropy ratio of $1000 : 1$ at 30° orientation, over the whole domain including the fractures. The matrix and the fractures are assigned the permeability of $\boldsymbol{K_m} = \left(\begin{smallmatrix} 0.75025 & 0.43258 \\ 0.43258 & 0.25075 \end{smallmatrix} \right)$ mD and $\boldsymbol{K_f} = 10^6 \times \boldsymbol{K_m}$, respectively. Fig. 34 shows pressure solutions solved via the hybrid-grid FPS method and the (FPS) 1D fracture model. The respective tracer concentration profiles are also given. Variations of tracer concentration at the producer versus time, for both the models, are shown in Fig. 38c. There is a significant discrepancy in the results obtained via the (FPS) 1D fracture model, when compared with the hybrid-grid FPS method for this case. As noted above, the 1D fracture model is consistent if the permeability tensor is diagonal in the local frame of the fracture. Consequently having a strong anisotropic full-tensor permeability in the fractures leads to an O(1) error which explains the discrepancy in results.

6.2.4. Case 6d: Strong full-tensor ($1000 : 1$ at 30°) matrix field and diagonal tensor fracture field

The matrix is assigned a permeability tensor $\boldsymbol{K_m} = \left(\begin{smallmatrix} 0.75025 & 0.43258 \\ 0.43258 & 0.25075 \end{smallmatrix} \right)$ mD. The fractures are assigned a diagonal isotropic permeability field of $\boldsymbol{K_f} = 10^6 \times \boldsymbol{I}$ mD. For this case the 1D fracture model is consistent and results of the 1D fracture model conform to the results obtained by the hybrid-grid FPS method, as
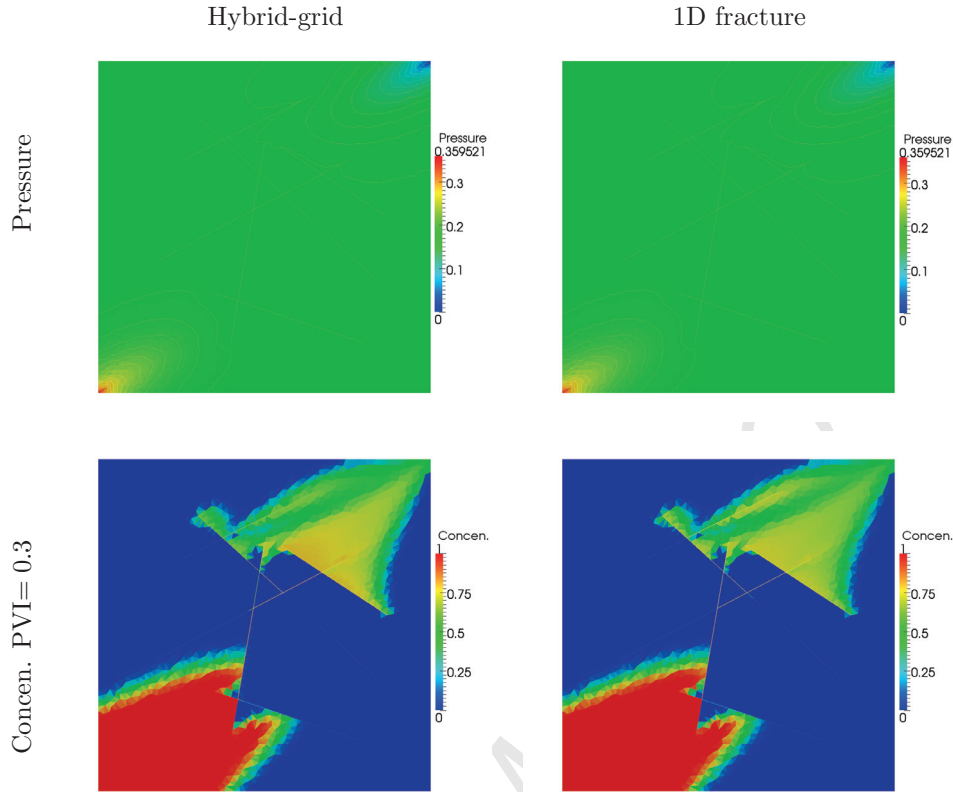
40

Figure 33: Case 6b: Pressure solution and tracer concentration contours (PVI= 0.3) obtained by the hybrid-grid FPS and the (FPS) 1D fracture model for an anisotropic (10 : 1 at 30°) full-tensor field over a domain with multiple intersecting fractures.

shown in Fig. 35 and Fig. 38d.

6.2.5. Case 6e: Very strong full-tensor field ($3000 : 1$ at 25°)

The next case considers a very strong anisotropic full-tensor permeability field ($3000 : 1$ at 25°) over the whole domain. The matrix permeability tensor is defined by $\boldsymbol{K_m} = \left(\begin{smallmatrix} 0.246436 & .114868 \\ .114868 & 0.053664 \end{smallmatrix} \right)$ mD and the fracture permeability is defined by $\boldsymbol{K_f} = 10^6 \times \boldsymbol{K_m}$. Fig. 36 shows the pressure fields and the respective tracer concentration contours obtained via the hybrid-grid FPS method and the 1D fracture model. Variations of concentration at producer with respect to time, for both the models, are shown in Fig. 38e. Again, there is a significant difference in the results obtained via the (FPS) 1D fracture model and the hybrid-grid FPS method which is due to the 1D fracture model being inconsistent when a very strong anisotropic full-tensor permeability field is present in the fractures.

6.2.6. Case 6f: Very strong full-tensor ($3000 : 1$ at 25°) matrix field and diagonal tensor fracture field

Lastly, we consider the matrix with a very strong anisotropic full-tensor permeability field ($3000 : 1$ at 25°) while the fractures are assigned an diagonal isotropic permeability field $\boldsymbol{K_f} = 10^6 \times \boldsymbol{I}$. Fig. 37 shows the pressure solutions and the respective tracer concentration contours obtained via the hybrid-grid FPS method
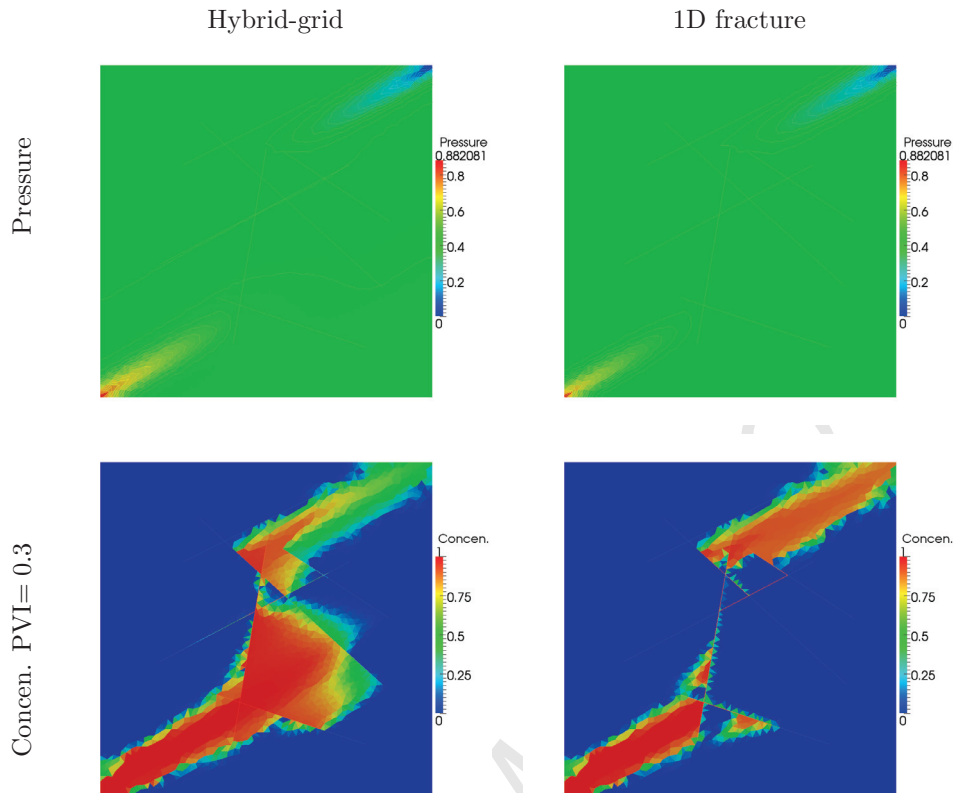
Figure 34: Case 6c: Pressure solution and tracer concentration contours (PVI= 0.3) obtained by the hybrid-grid FPS and the (FPS) 1D fracture model for an anisotropic (1000 : 1 at 30°) full-tensor field over a domain with multiple intersecting fractures.

660 and the 1D fracture model. Fig. 38f shows the plots of tracer concentration at the producer with respect to time for both the models. For this case with diagonal isotropic permeability tensor in the fractures, the 1D model is again consistent and the results of the 1D fracture model conform to the results obtained via the hybrid-grid FPS method as in the previous case of an anisotropic (1000 : 1 at 30°) matrix and diagonal isotropic tensor in the fractures.

665 All of the above test cases involving the various permeability fields, for the injector-producer problem, show that FPS coupled with the lower-dimensional fracture model yields results that are in good agreement with the hybrid-grid FPS method when the fracture permeability tensor is diagonal or even has a weak full-tensor while the matrix can have a full-tensor of arbitrary strength.

Finally, we consider the channel flow problem of section 5.6 again, and solve using FPS coupled with the
670 lower-dimensional (1D) fracture model. We compute the computational cost of TPS and FPS coupled with 1D fracture model compared to the hybrid-grid TPS and FPS methods for the channel flow problem using the mesh as shown in Fig. 25b. Table 2 shows the computational costs of different methods used for the problem of all fractures in the domain. There is no considerable difference in both the models with TPS and FPS for the fracture system.
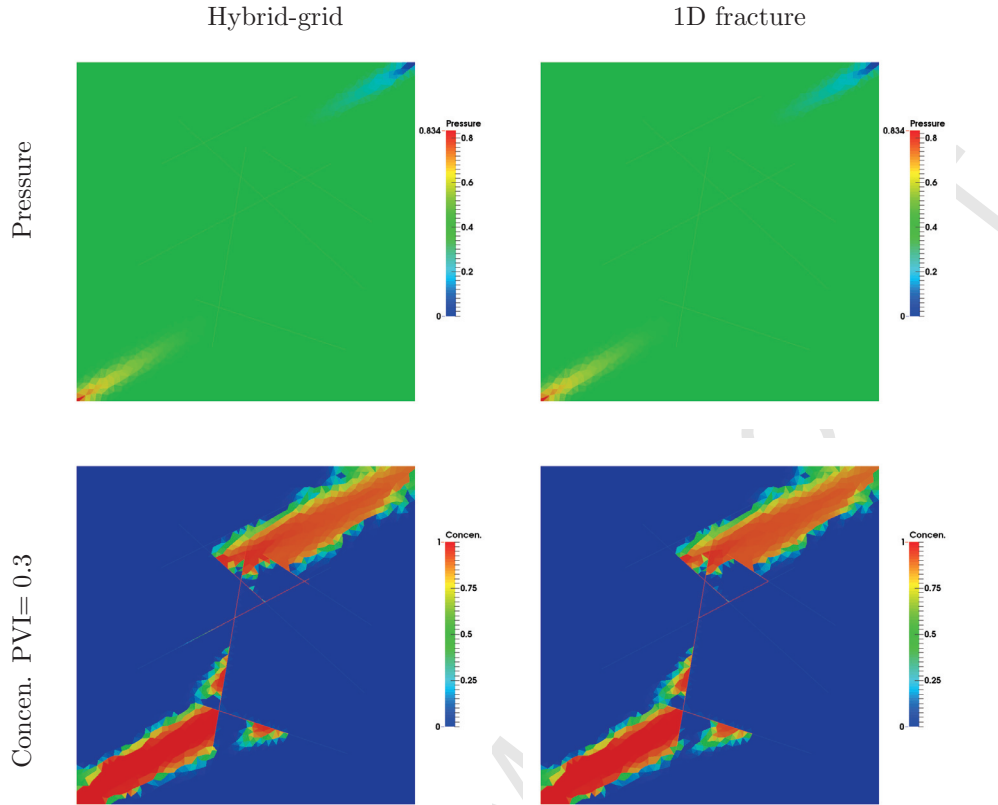
42

Figure 35: Case 6d: Pressure solution and tracer concentration contours (at PVI= 0.3) obtained by the hybrid-grid FPS and the (FPS) 1D fracture model for an anisotropic ($1000 : 1$ at 30°) full-tensor field over matrix with multiple intersecting fractures with diagonal isotropic permeability.

Fracture model	TPS	FPS
Hybrid-grid model	1.11	1.15
1D fracture model	1.11	1.12

Table 2: Case 4: CPU time (sec) for the hybrid-grid TPS and FPS and the 1D fracture model with TPS and FPS for a fracture system with $a = 1$ mm and $k_f = 10^6$. The linear system is solved by GMRES preconditioned by algebraic multi-grid (*gamg* provided in PETSc, rtol = 1e-10).

7. Conclusions

Two novel control-volume methods are presented for flow in fractured media, and involve coupling the cell-centred CVD-MPFA full pressure support formulation, to two types of discrete fracture-matrix approximation for simulation on unstructured grids. First, we introduce the hybrid-grid FPS method for DFM simulations. We present a novel and simple process to form a consistent hybrid-grid locally for a dual-cell. We also present a novel hybrid-grid for the application of the FPS scheme to intersecting fractures, with full pressure continuity imposed along the matrix-matrix, matrix-fracture and fracture-fracture interfaces.

Convergence rates of the hybrid-grid FPS method overlay the hybrid-grid TPS scheme and are in excellent agreement when hybrid-grid TPS is effective. Comparison of pressure and transport solutions computed by both the TPS and FPS hybrid-grid methods are presented for diagonal and full-tensor permeability fields on
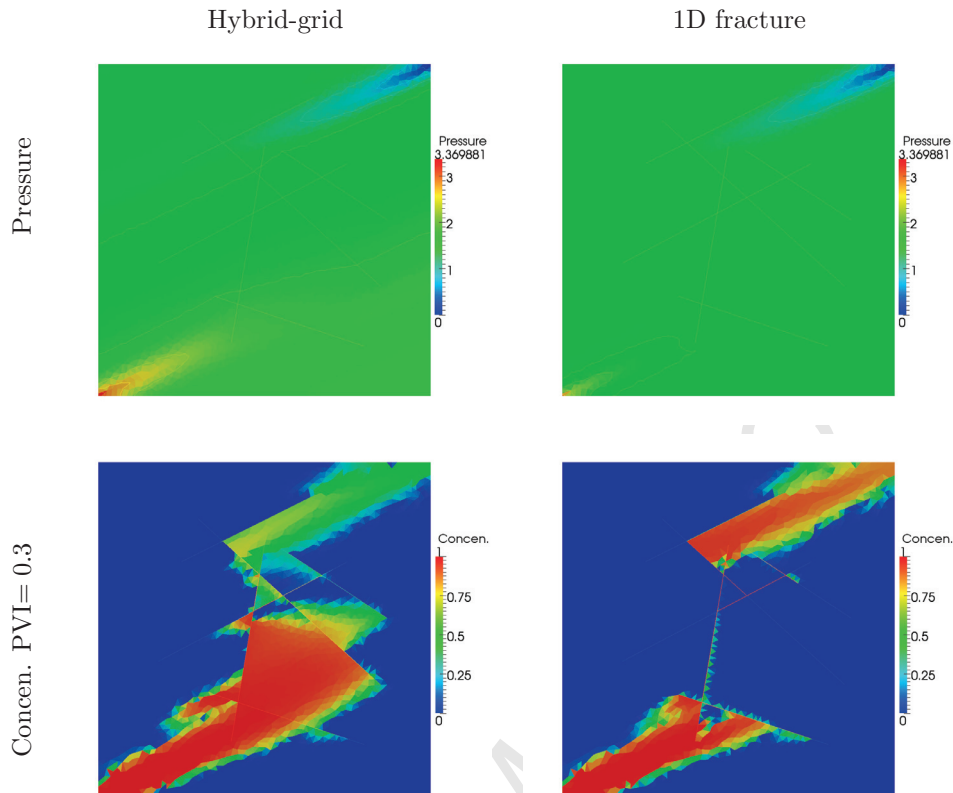
43

Figure 36: Case 6e: Pressure solution and tracer concentration contours (PVI= 0.3) obtained by the hybrid-grid FPS and the (FPS) 1D fracture model for an anisotropic (3000 : 1 at 25º) full-tensor field over a domain with multiple intersecting fractures.

685 unstructured meshes. When compared to the reference solutions, hybrid-grid FPS yields improved results for fractured domains in contrast to the hybrid-grid TPS scheme. The hybrid-grid FPS method is highly beneficial for fractured domains with very strong anisotropic full-tensor permeability fields, and yields well resolved pressure solutions. In contrast the TPS formulation yields pressure solutions with strong spurious oscillations for such cases. A transient pressure simulation of compressible gas flow has also been presented

690 for a complex discrete fracture-matrix system. The hybrid-grid TPS simulation fails for this case, while the FPS results demonstrate the applicability of the newly developed hybrid-grid FPS method for transient drainage of fractured zones involving compressible flow in complex fracture networks.

A lower-dimensional fracture model is efficiently coupled with FPS. A comparison of transport solutions obtained via FPS coupled with the lower-dimensional fracture model and the hybrid-grid FPS method is

695 presented. FPS coupled with the lower-dimensional fracture model is consistent for an arbitrary general tensor (full or diagonal) in the matrix and a strictly diagonal tensor of arbitrary anisotropy ratio in the local frame of the fracture. Results are computed for a range of full-tensor permeability fields in the matrix and fractures, and contrasted with results for the same matrix properties, and with the same geometric fractures assigned a locally diagonal permeability tensor field. For a strong full-tensor field in the fracture, the $O(1)$

700 error in the lower dimensional model approximation leads to an erroneous pressure field due to omission of
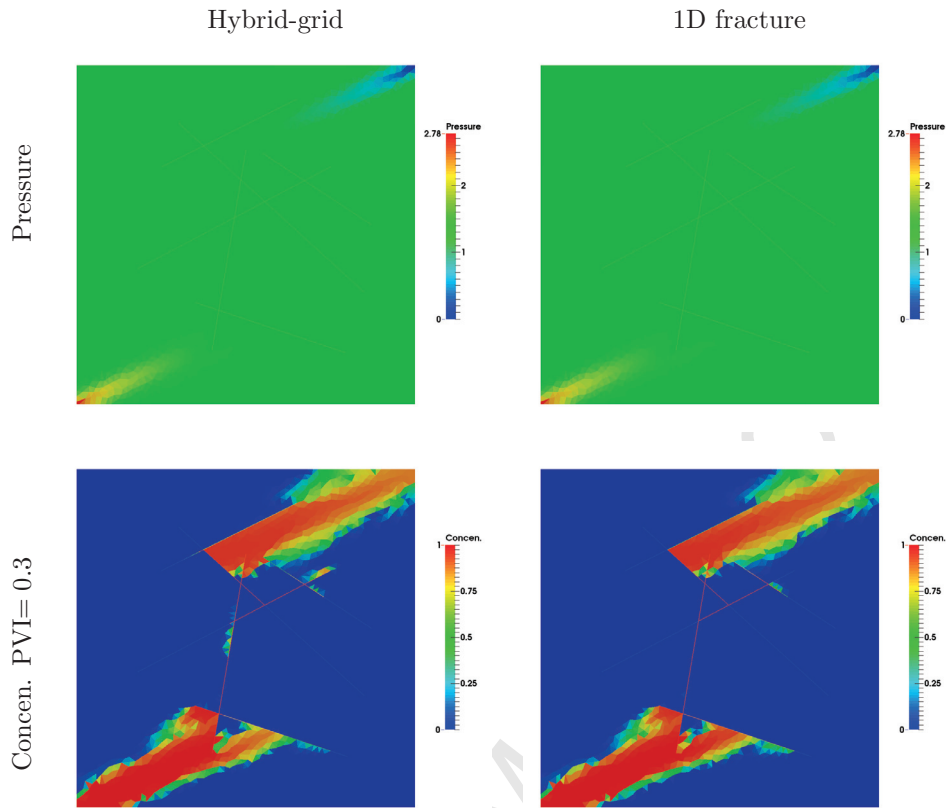
44

Figure 37: Case 6f: Pressure solution and tracer concentration contours (PVI= 0.3) obtained by the hybrid-grid FPS and the (FPS) 1D fracture model for an anisotropic (3000 : 1 at 25°) full-tensor field over matrix with multiple intersecting fractures with diagonal isotropic permeability.

the second dimension in the reduced dimensional fracture model. The O(1) error, due to the 1D fracture assumption, reduces with reduction in strength of the full-tensor field in the fracture, restoring consistency of the lower-dimensional method as the off-diagonal tensor coefficient reduces to zero in the fracture. The results also show that FPS coupled with the lower-dimensional fracture model yields solutions comparable to the hybrid-grid FPS method, when the permeability tensor of the conducting fractures is locally diagonal or even with a full-tensor having a weak off-diagonal coefficient.
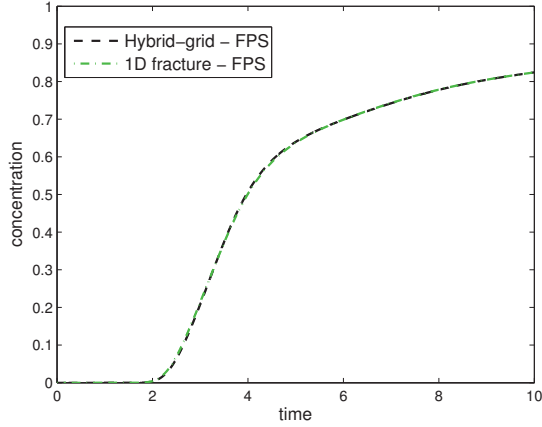
(a) Isotropic
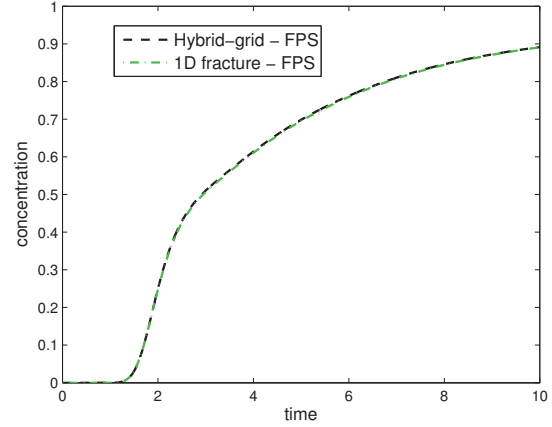
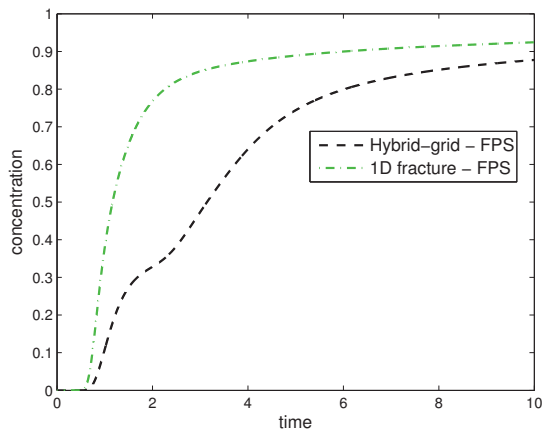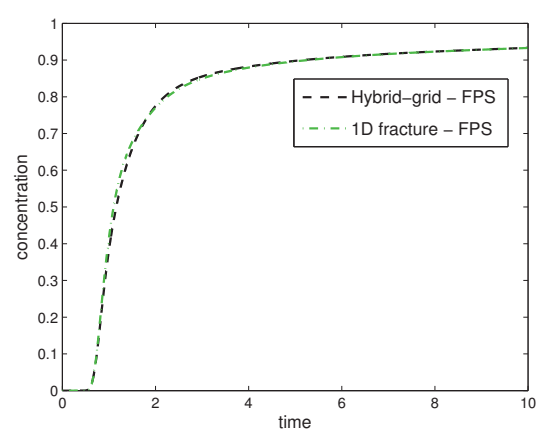(b) Anisotropic $10 : 1$ at 30°
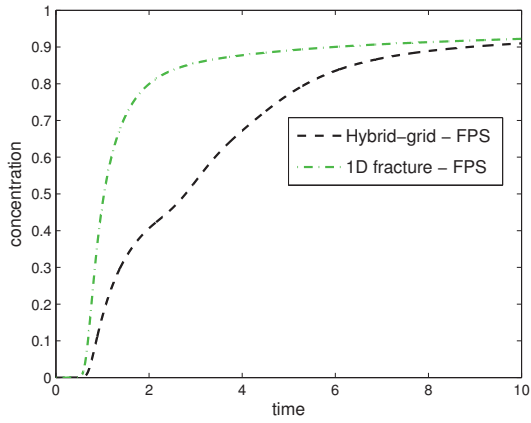
(c) Anisotropic $1000 : 1$ at 30°
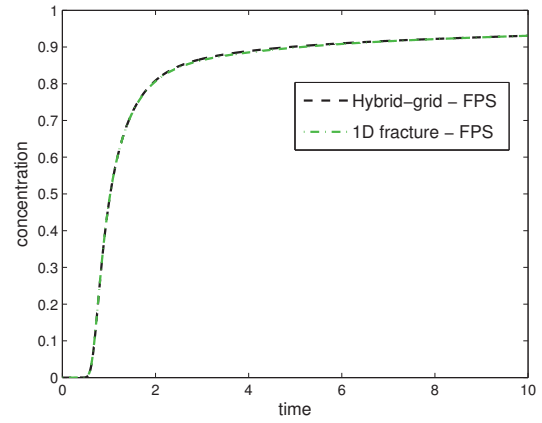
(d) Anisotropic ($1000 : 1$ at 30°) matrix and isotropic fractures

(e) Anisotropic $3000 : 1$ at 25°

(f) Anisotropic ($3000 : 1$ at 25°) matrix and isotropic fractures

Figure 38: Case 6: Tracer concentration at producer versus time (years) solved by the hybrid-grid FPS and the FPS coupled with the (FPS) 1D fracture model

Appendix A. Nomenclature

ϕ	pressure
Φ	vector of pressures
φ	porosity
μ	viscosity
a	fracture aperture
c	tracer concentration
c_t	total compressibility
CVD-MPFA	control-volume distributed multi-point flux approximation
DFM	discrete-fracture model
F	flux
$\mathcal{F}$	1D fracture-fracture flux
$\boldsymbol{k}$	permeability tensor
$\boldsymbol{K}$	$\frac{\boldsymbol{k}}{\mu}$
M	molecular weight of a gas
Q_f	transfer function
q	quadrature of CVD-MPFA schemes
q_c	known source term
R	ideal gas constant
Z	gas compressibility factor

Subscripts

m	matrix
f	fracture

Superscript

tr	transpose

References

[1] J. Noorishad, M. Mehran, An upstream finite element method for solution of transient transport equation in fractured porous media, Water Resour. Res. 18 (03) (1982) 588–596.

[2] R. Baca, R. Arnett, D. Langford, Modeling fluid flow in fractured porous rock masses by finite element techniques, Int. J. Numer. Methods Fluids 04 (04) (1984) 337–348.

[3] M. F. Lough, S. H. Lee, J. Kamath, An efficient boundary integral formulation for flow through fractured porous media, J. Comput. Phys. 143 (2) (1998) 462–483.

[4] S. H. Lee, M. F. Lough, C. L. Jensen, Hierarchical modeling of flow in naturally fractured formations with multiple length scales, Water Resour. Res. 37 (03) (2001) 443–455.

[5] M. Karimi-Fard, A. Firoozabadi, Numerical simulation of water injection in fractured media using the discrete-fracture model and the Galerkin method, SPE Reserv. Eval. Eng. 6 (02) (2003) 117–126.

47

[6] M. Karimi-Fard, L. J. Durlofsky, K. Aziz, An efficient discrete-fracture model applicable for general-purpose
725   reservoir simulators, SPE J. 09 (02) (2004) 227–236.

[7] V. Martin, J. Jaffré, J. E. Roberts, Modelling fractures and barriers as interfaces for flow in porous media, SIAM
    J. Sci. Comput. 26 (2005) 1667–1691.

[8] V. Reichenberger, H. Jakobs, P. Bastian, R. Helmig, A mixed-dimensional finite volume method for two-phase
    flow in fractured porous media, Adv. Water Resour. 29 (07) (2006) 1020–1036.

730 [9] S. K. Matthäi, A. Mezentsev, M. Belayneh, Finite-element node-centered finite-volume experiments with frac-
    tured rock represented by unstructured hybrid element meshes, SPE Reserv. Evalu. Eng 10 (6) (2007) 740–756.

[10] H. Hoteit, A. Firoozabadi, An efficient numerical model for incompressible two-phase flow in fractured media,
    Adv. Water Resour. 31 (06) (2008) 891–905.

[11] A. Paluszny, S. K. Matthäi, M. Hohmeyer, Hybrid finite element–finite volume discretization of complex geologic
735   structures and a new simulation workflow demonstrated on fractured rocks, Geofluids 7 (2) (2007) 186–208.

[12] H. Hajibeygi, D. Karvounis, P. Jenny, A hierarchical fracture model for the iterative multiscale finite-volume
    method, J. Comput. Phys. 230 (24) (2011) 8729–8743.

[13] V. Girault, M. F. Wheeler, B. Ganis, M. E. Mear, A lubrication fracture model in a poro-elastic medium, Math.
    Models Methods Appl. Sci. 25 (04) (2015) 587–645.

740 [14] G. Barenblatt, Y. Zheltov, I. Kochina, Basic concepts in the theory of seepage of homogeneous fluids in fissurized
    rocks, PMM(Soviet Appl. Math. Mech.) 24 (05) (1960) 852–864.

[15] J. Warren, P. Root, The behavior of naturally fractured reservoirs, SPE J. 03 (03) (1963) 245–255.

[16] H. Kazemi, L. S. Merrill, K. L. Porterfield, P. R. Zeman, Numerical simultion of water-oil flow in naturally
    fractured reservoirs, SPE J. 16 (06) (1976) 317–326.

745 [17] J. R. Gilman, Practical aspects of simulation of fractured reservoirs, in: International Forum on Reservoir
    Simulation, Buhl, Baden-Baden, Germany, 2003.

[18] B. T. Mallison, M. H. Hui, W. Narr, Practical gridding algorithms for discrete fracture modeling workflows, in:
    12th European Conference on the Mathematics of Oil Recovery, EAGE, 2010.

[19] H. Mustapha, R. Dimitrakopoulos, T. Graf, A. Firoozabadi, An efficient method for discretizing 3D fractured
750   media for subsurface flow and transport simulations, Int. J. Numer. Methods Fluids 67 (5) (2011) 651–670.

[20] H. Hægland, A. Assteerawatt, H. K. Dahle, G. T. Eigestad, R. Helmig, Comparison of cell- and vertex-centered
    discretization methods for flow in a two-dimensional discrete-fracture-matrix system, Adv. Water Resour. 32 (12)
    (2009) 1740–1755.

[21] C. D. Foster, T. M. Nejad, Embedded discontinuity finite element modeling of fluid flow in fractured porous
755   media, Acta Geotechnica 8 (1) (2013) 49–57.

[22] C. D'Angelo, A. Scotti, A mixed finite element method for Darcy flow in fractured porous media with non-
    matching grids, ESAIM: Math. Model. Numer. Anal. 46 (2012) 465–489.

[23] S. Berrone, S. Pieraccini, S. Scialò, An optimization approach for large scale simulations of discrete fracture
    network flows, J. Comput. Phys. 256 (2014) 838–853.

760 [24] J. Moortgat, A. Firoozabadi, Higher-order compositional modeling of three-phase flow in 3D fractured porous
    media based on cross-flow equilibrium, J. Comput. Phys. 250 (2013) 425 – 445.

[25] A. Zidane, A. Firoozabadi, An efficient numerical model for multicomponent compressible flow in fractured
    porous media, Adv. Water Resour. 74 (2014) 127–147.

[26] A. Zidane, A. Firoozabadi, An implicit numerical model for multicomponent compressible two-phase flow in
765   porous media, Adv. Water Resour. 85 (2015) 64–78.

[27] J. Moortgat, M. A. Amooie, M. R. Soltanian, Implicit finite volume and discontinuous Galerkin methods for
    multicomponent flow in unstructured 3D fractured porous media, Adv. Water Resour. 96 (2016) 389–404.

[28] O. Al-Hinai, S. Srinivasan, M. F. Wheeler, Mimetic finite differences for flow in fractures from microseismic data, in: SPE Reservoir Simulation Symposium, Society of Petroleum Engineers, 2015.

[29] R. Masson, K. Brenner, M. Groza, L. Jeannin, J. F. Thebault, Vertex approximate gradient scheme for hybrid dimensional two-phase darcy flows in fractured porous media, in: ECMOR XIV-14th European conference on the mathematics of oil recovery, 2014.

[30] K. Brenner, M. Groza, G. Guichard, C.and Lebeau, R. Masson, Gradient discretization of hybrid dimensional darcy flows in fractured porous media, in: Finite Volumes for Complex Applications VII-Elliptic, Parabolic and Hyperbolic Problems, Springer, 2014, pp. 527–535.

[31] T. H. Sandve, I. Berre, J. M. Nordbotten, An efficient multi-point flux approximation method for discrete fracture-matrix simulations, J. Comput. Phys. 231 (09) (2012) 3784–3800.

[32] I. Aavatsmark, T. Barkve, O. Bøe, T. Mannseth, Discretization on unstructured grids for inhomogeneous, anisotropic media. Part I: Derivation of the methods, SIAM J. Sci. Comput. 19 (5) (1998) 1700–1716.

[33] R. Ahmed, M. G. Edwards, S. Lamine, B. A. H. Huisman, M. Pal, Control-volume distributed multi-point flux approximation coupled with a lower-dimensional fracture model, J. Comput. Phys. 284 (2015) 462–489.

[34] R. Ahmed, M. G. Edwards, S. Lamine, B. A. H. Huisman, M. Pal, Three-dimensional control-volume distributed multi-point flux approximation coupled with a lower-dimensional surface fracture model, J. Comput. Phys. 303 (2015) 470–497.

[35] M. G. Edwards, C. F. Rogers, Finite volume discretization with imposed flux continuity for the general tensor pressure equation, Comput. Geosci. 02 (04) (1998) 259–290.

[36] H. A. Friis, M. G. Edwards, J. Mykkeltveit, Symmetric positive definite flux-continuous full-tensor finite-volume schemes on unstructured cell-centered triangular grids, SIAM J. Sci. Comput. 31 (02) (2008) 1192–1220.

[37] I. Aavatsmark, An introduction to multipoint flux approximations for quadrilateral grids, Comput. Geosci. 06 (3-4) (2002) 405–432.

[38] M. F. Wheeler, I. Yotov, A multipoint flux mixed finite element method, SIAM J. Numer. Anal. 44 (5) (2006) 2082–2106.

[39] S. Lee, L. Durlofsky, M. Lough, W. Chen, Finite difference simulation of geologically complex reservoirs with tensor permeabilities, SPE Reserv. Eval. Eng. 01 (1998) 567–574, sPE-52637-PA.

[40] M. G. Edwards, H. Zheng, A quasi-positive family of continuous Darcy-flux finite-volume schemes with full pressure support, J. Comput. Phys. 227 (22) (2008) 9333–9364.

[41] M. G. Edwards, H. Zheng, Double-families of quasi-positive Darcy-flux approximations with highly anisotropic tensors on structured and unstructured grids, J. Comput. Phys. 229 (03) (2010) 594–625.

[42] H. A. Friis, M. G. Edwards, A family of MPFA finite-volume schemes with full pressure support for the general tensor pressure equation on cell-centered triangular grids, J. Comput. Phys. 230 (01) (2011) 205–231.

[43] I. Aavatsmark, G. Eigestad, B. Mallison, J. Nordbotten, A compact multipoint flux approximation method with improved robustness, Numer. Meth. Part. Differ. Equations 24 (5) (2008) 1329–1360.

[44] Q.-Y. Chen, J. Wan, Y. Yang, R. Mifflin, Enriched multi-point flux approximation for general grids, J. Comput. Phys. 227 (3) (2008) 1701–1721.

[45] K. Lipnikov, D. Svyatskiy, Y. Vassilevski, Minimal stencil finite volume scheme with the discrete maximum principle, Russ. J. Numer. Anal. Math. Modelling 27 (4) (2012) 369–385.

[46] D. Kuzmin, M. Shashkov, D. Svyatskiy, A constrained finite element method satisfying the discrete maximum principle for anisotropic diffusion problems, J. Comput. Phys. 228 (2009) 3448–3463.

[47] M. Karimi-Fard, A. Firoozabadi, Numerical simulation of water injection in 2D fractured media using discrete-fracture model, in: SPE Annual Technical Conference and Exhibition, SPE, 2001.

[48] J. R. Shewchuk, Triangle: Engineering a 2D Quality Mesh Generator and Delaunay Triangulator, in: Applied Computational Geometry: Towards Geometric Engineering, Vol. 1148 of Lecture Notes in Computer Science, Springer-Verlag, 1996, pp. 203–222.

[49] D.-Y. Peng, D. B. Robinson, A new two-constant equation of state, Ind. Eng. Chem. Fundam. 15 (1) (1976) 59–64.

[50] N. Böttcher, A.-K. Singh, O. Kolditz, R. Liedl, Non-isothermal, compressible gas flow for the simulation of an enhanced gas recovery application, J. Comput. Appl. Math. 236 (18) (2012) 4933–4943.

[51] L. P. Dake, Fundamentals of reservoir engineering, Elsevier, 1983.

[52] S. Balay, M. F. Adams, J. Brown, P. Brune, K. Buschelman, V. Eijkhout, W. D. Gropp, D. Kaushik, M. G. Knepley, L. C. McInnes, K. Rupp, B. F. Smith, H. Zhang, PETSc Web page, http://www.mcs.anl.gov/petsc (2015).

[53] Y. Saad, M. H. Schultz, Gmres: A generalized minimal residual algorithm for solving nonsymmetric linear systems, SIAM J. Sci. Stat. Comput. 7 (3) (1986) 856–869.

[54] D. G. Friend, J. F. Ely, H. Ingham, Thermophysical properties of methane, J. Phys. Chem. Ref. Data 18 (2) (1989) 583–638.